PMUT reconfigure bandwidth by using electronic feedback

MSc thesis project

Maodong Yang

PMUT reconfigure bandwidth by using electronic feedback

by

Maodong Yang

to obtain the degree of Master of Science
at the Delft University of Technology,
to be defended publicly on Thursday October 31, 2024 at 14:00 PM.

Student number:	5656478	
Project duration:	September 1, 2023 – October 31, 2024	
Thesis committee:	dr. T. Manzaneque,	TU Delft, supervisor
	dr. T. Costa,	TU Delft
	Xiaoxi Zhao,	TU Delft

TU Delft

Abstract

Piezoelectric micromachined ultrasonic transducers (PMUTs) are commonly employed in applications such as medical imaging and gesture recognition. One important performance metric for PMUTs is the quality factor. However, once fabricated, PMUTs have fixed parameters, making them non-tunable for adaptation to various scenarios. This paper presents a technique for using feedback circuits to regulate the bandwidth and quality factor of PMUTs, thereby broadening the potential applications for fabricated PMUTs. First, the electrical characterization of a ScAlN-based PMUT was implemented to extract the parameters in the Butterworth-Van Dyke (BVD) model, which was used in the circuit design simulations.

Second, the circuit was designed to control the quality factor and bandwidth, simply by adjusting variable resistors in the feedback loop. The characterization results of PCB validated the function of the design. The difference with simulation results was analyzed. Finally, the ultimate performance of the circuit was characterized by a wire-bonded PMUT. The results show that the proposed circuit design effectively manages the Q-factor from 279 to 576 in the quality factor increasing circuit, and 279 to 180 in the quality factor decreasing circuit.

Contents

List of Figures

List of Tables

1 Introduction

1.1. Applications of ultrasound transducers

Ultrasound finds applications across a diverse spectrum of life, including consumer markets, automotive, as well as industrial sectors, and medical fields. The consumer market includes fingerprint sensors and gesture recognition, the automotive market includes parking assistance, the industrial market includes automation and non-destructive testing, and the medical market includes medical ultrasound imaging and therapeutic applications.

1.2. Medical ultrasound basic principle

Medical imaging includes various technologies employed to observe the human body to diagnose, monitor, or treat medical conditions. These technologies encompass X-ray, ultrasound, Magnetic Resonance Imaging, nuclear imaging, microscopy, and others[41]. Each imaging modalities have different advantages and working principles.

Among these technologies, X-ray stands out as the most commonly used. X-rays belong to the group of electromagnetic rays, and when these rays traverse various materials, the materials absorb some energy. The distinct absorption behaviors result in different energy losses for different materials. Consequently, X-ray radiography reveals specific contrasts in the image, arising from variations in energy loss [5]. However, X-ray imaging and other ionizing radiation modalities can also be harmful, the absorbed energy from medical imaging radiation exposure into human tissue will have a low risk of developing cancer and other side effects [2]. The following technology is ultrasound imaging, which ranks as the second most widely employed modality, with over 25% of medical imaging procedures involving ultrasound [19]. Unlike X-rays, ultrasound imaging has a different working principle, it uses ultrasound waves to view inside the body. It has been employed in medical applications since the 1950s and does not have the same side effects as X-ray [30].

Audible acoustic sound waves encountered in life are usually produced by the vibration sources in the air. Similar to audible sound waves, ultrasound waves are generated by the vibration of piezoelectric crystals. However, ultrasound waves have frequencies beyond what the human ear can hear which exceeds 20KHz. For diagnostic purposes, two main techniques are utilized in medical ultrasound: the Doppler effect and the pulse-echo method. The Doppler technique relies on the principle that ultrasound echoes reflected from a moving target experience a change in their frequency. And it is used to assess tissue movement and blood flow [30]. In the pulse-echo method of ultrasound imaging, the ultrasound transducer with piezoelectric material produces pulses transmitted into the body. As the sound waves cross diverse mediums, phenomena such as attenuation, reflection, and scattering occur. As the sound wave reflects off body tissues, the variation in reception times and speed of sound in the medium allow for the determination of the distance between tissues. It is used to create images of tissue distribution.

1.3. Medical ultrasound imaging generation and important metrics

Based on the pulse-echo method, the image presented returning echoes in a one-dimensional graphical format can be obtained, and it is referred to as amplitude mode or A-mode. However, sound waves will attenuate when they pass through body tissues. Figure 1.1 shows the reduced amplitude of the reflected waves. This is because part of the energy of the ultrasonic wave is absorbed by the medium. The attenuation coefficient depends on the frequency and the material, specifically, the attenuation is quantified in 1–2 dB/cm/MHz [56]. Based on the attenuation coefficient, high-frequency sound waves will experience greater acoustic energy loss when penetrating the same depth of body tissue compared to low-frequency sound waves. However, high-frequency sound waves were deemed essential for distinguishing between biological tissues.[63].

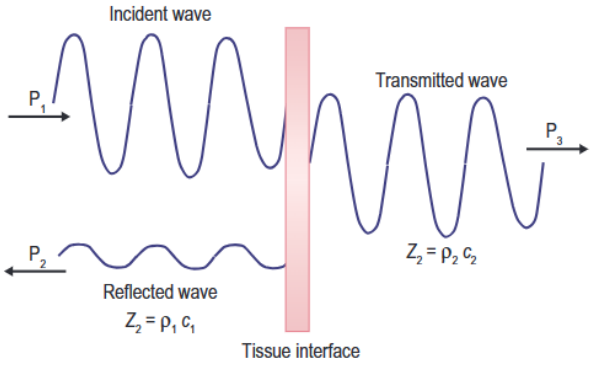

Figure 1.1: Ultrasound waves reflection and transmission(Z is the acoustic impedance in the medium, ρ and c are the density and speed of sound in the medium). Reprinted from[10]

In addition to A-mode, another type of ultrasound imaging is B-mode. B-mode, short for brightness mode, employing an array of transducer elements enables the emission of sequential ultrasound pulses in different directions to create multiple image lines, resulting in a two-dimensional image. The different brightnesses are determined by the amplitude peaks of the returned echo[30]. A B-mode image is shown in figure 1.3. To form a good-quality ultrasound image, the resolution of an image is important. The resolution in the image can be defined in lateral resolution and axial resolution. The lateral resolution refers to the capacity to differentiate distinct structures situated perpendicular, or laterally, to the beam axis [39]. The beam results from the combination of ultrasound waves emitted by transducer elements in various directions. Greater lateral resolution is achieved with a narrower beam width. A narrower beam width is associated with a higher frequency[39]. The axial resolution denotes the ability to distinguish the longitudinal separation between two objects[39]. Axial resolution equals half of the spatial pulse length, implying that a shorter spatial pulse length results in improved axial resolution. Because the spatial pulse length is inversely proportional to the bandwidth. An ultrasound transducer with a wide bandwidth can generate shorter spatial pulse length[49]. However, the exact mathematical relationship between the general signal of ultrasound waves from the time domain to the frequency domain is complicated. The relationship can still be explained roughly by a Fourier transform scaling theorem[52]:

$$\mathscr{F}\{g(at)\} = \frac{1}{|a|}G(\frac{f}{a}) \tag{1.1}$$

where the t (time) can be seen as the length of a single pulse, and a is the number of cycles. It indicates a reciprocal relationship between time “length” and frequency “length”. The figure 1.2 shows the same conclusion.

Penetration depth and resolution are two important metrics to measure the quality of ultrasound equipment. Due to the attenuation of sound waves in human tissue, there is a limitation to using high-frequency sound waves to get a high-resolution image. Therefore, increasing the pulse bandwidth is another option to increase the axial resolution of the ultrasound image. Generally, ultrasound transducers require different working resonance frequencies, ranging from 1 to 20MHz, to comprise the conflict of penetration depth and resolution[56]. Another important metric to improve the ultrasound image

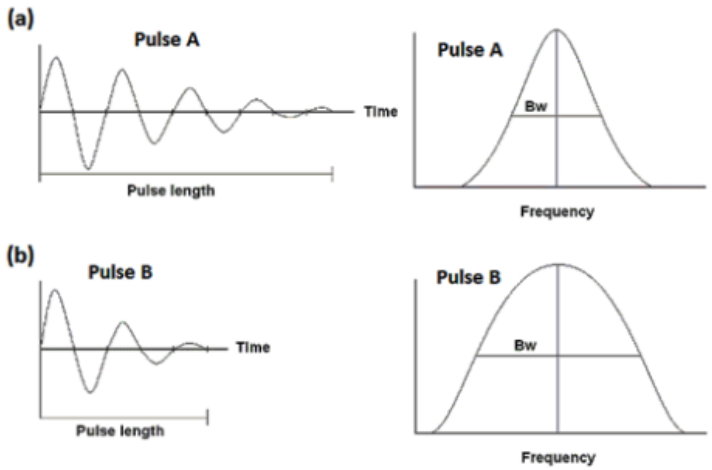

Figure 1.2: (a) Longer pulse (Pulse A) in time domain and frequency domain and; (b) Shorter pulse (Pulse B) in time domain and frequency domain. Reprinted from[60]

quality is the sensitivity of the transducer. The sensitivity will influence the contrast ratio of the image. A transducer with higher sensitivity can produce a more vivid image of the target[29]. However, in ultrasound transducer design, there is always a trade-off between sensitivity and bandwidth. The increasing sensitivity always causes a reduction in bandwidth. In ultrasound imaging, it means the conflicts between the contrast ratio and resolution of the image.

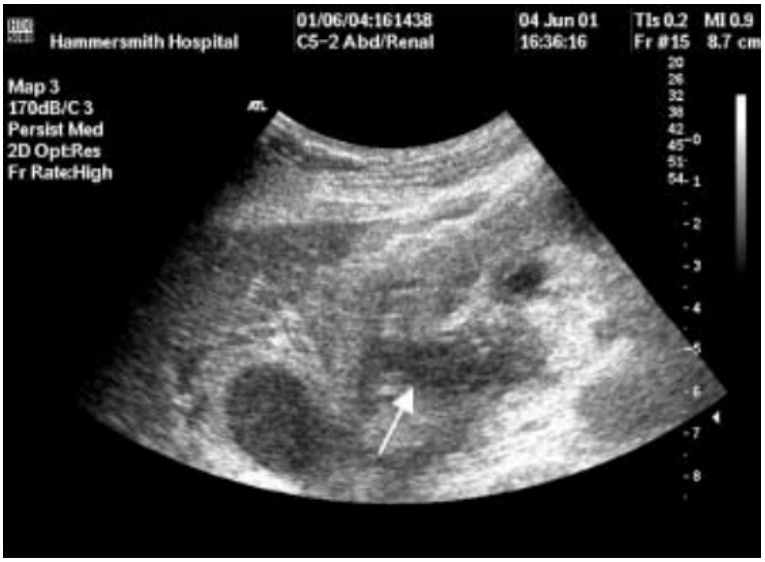

Figure 1.3: The B-mode image shows an ill-defined lesion in the pancreatic head (arrow). Reprinted from[18]

2

Piezoelectric MEMS resonator theory

2.1. Piezoelectricity

The ultrasound transducers used in medical ultrasound imaging rely on electromechanical transduction, converting mechanical energy to electrical energy and vice versa. The primary mechanism for this energy conversion is piezoelectricity. The term "Piezoelectricity" originates from Greek and translates to "electricity by pressure." And it indicates that Piezoelectricity is a convergence of various classical scientific fields, encompassing mechanics, elasticity and strength of materials, acoustics, wave propagation, electrostatics, and more[4].

However, not every material has a piezoelectric effect. When mechanical stress is applied to centrosymmetric crystals, it gives rise to a symmetry group that includes a center of symmetry. This implies that after any uniform deformation, a centrosymmetric crystal maintains its centrosymmetry[42]. So, in a symmetric structure with the gravity centers of the negative and positive charges within each molecule aligned, the external effects of the negative and positive charges mutually cancel each other, shown in figure 2.1 a, hence, there is no accumulation of electric charge, and materials of this kind do not exhibit the piezoelectric effect.

(a) A centrosymmetric crystal structure cannot show piezoelectricity.

(b) A non-centrosymmetric crystal structure shows piezoelectricity.

Figure 2.1: Centrosymmetric crystal structure and non-centrosymmetric crystal structure Reprinted from[46]

For a non-centrosymmetric crystal structure (figure2.1 b), mechanical stress induces electric polarization, and conversely, an applied electric field generates mechanical strain. And it can be expressed in the following equations[8]:

$$D_i = d_{ij}\sigma_j + \varepsilon^{\sigma}_{ij}E_j \tag{2.1}$$

$$\epsilon_i = s^{E}_{ij}\sigma_j + d^{t}_{ij}E_j \tag{2.2}$$

D represents the displacement electric field in the form of 1×3 column matrix, d represents piezoelectric coefficients in the form of of3×6 vectors, and the superscript t in the d^t stands for transposition of the matrix. σ and ϵ are stress and strain respectively and they are 1×6 column matrices. ε^{σ} indicates

permittivity coefficients with 3×3 matrix under constant stress. E represents a 1×3 electric field matrix. Similar to the compliance coefficient, the superscript E means that 6×6 compliance matrix is under the constant electric field. Within the piezoelectric coefficients matrix(d_{ij}), the subscripts i/j, represented by Arabic numerals from 1 to 6, denote elements that correspond to the Cartesian axes(i.e. x, y, z→ 1, 2, 3 and 11→ 1, 22→ 2, 33→ 3, 23→ 4, 13→ 5, 12→ 6) [21]. The first subscript indicates the direction of the electric field linked to the applied voltage, while the second subscript indicates the direction of mechanical strain[21].

Various piezoelectric materials exhibit distinct properties and have been developed and tested for diverse thin-film piezoelectric microelectromechanical systems (MEMS) devices. As the thin film material is deposited onto a substrate and experienced clamping, its material properties are significantly affected. To quantify the piezoelectric MEMS device performance with different thin-film piezoelectric materials, the piezoelectric constants of $e_{31,f}$ (effective piezoelectric stress coefficient) and $d_{33,f}$ (effective piezoelectric coefficient) are calculated by [21]:

$$e_{31,f} = \frac{d_{31}}{s_{11}^E + s_{12}^E} \equiv e_{31} - \frac{c_{13}^E}{c_{33}^E} e_{33} \tag{2.3}$$

$$d_{33,f} = \frac{e_{33}}{c_{33}^E} \equiv d_{33} - \frac{2s_{13}^E}{s_{11}^E + s_{12}^E} |d_{31}| \tag{2.4}$$

where c represents the stiffness and subscript f means thin film. From the equations above, it is evident that $|e_{31,f}| > |e_{31}|$ and $d_{33,f} < d_{33}$,indicating that thin-film-based piezoelectric MEMS devices hold an advantage in flexural mode (d31 mode). However, the piezoelectric constant is not the only parameter important for the piezoelectric MEMS device. For example, the dielectric loss ($tan\delta$) will produce a noise current or voltage, and place constraints on the resolution, specifically on the signal-to-noise ratio of MEMS devices[57]. The figure of merit of different materials is shown in table 2.1.

Figure of merit	Notation	PZT	ALN	$Sc_{0.5}ALN$	ZnO
in-plane deflection force	$\|e_{31,f}\|$	8-12	1.05	1.6	1
dielectric constant	$\varepsilon_{33,f}$	300-1300	10.5	12	10.9
piezoelectric voltage in deformed PMUTs	$\|e_{31,f}\|/\varepsilon_0\varepsilon_{33}$	0.7-1.8	11.3	15	10.3
coupling coefficient for flexural wave	$e_{31,f}^2/\varepsilon_0\varepsilon_{33}$	5.6-54.2	11.9	24	10.3
signal-to-noise-ratio	$\|e_{31,f}\|/(\varepsilon_0\varepsilon_{33}tan\delta)^{0.5}$	4-8	20	/	3-10

Table 2.1: Figure of merit of different materials. Reprinted from [45]

2.2. Piezoelectric MEMS lumped-element model theory

2.2.1. MEMS resonator parameters

Piezoelectric MEMS resonators function based on the phenomenon that involves the conversion of energy from the electrical domain to the mechanical domain and vice versa. In a conventional piezoelectric MEMS resonator, the piezoelectric material is sandwiched by two electrodes. The mechanical energy within the MEMS resonator body and the electrical energy applied through the metallic electrodes transform between potential and kinetic states in each half cycle of vibration[6]. The energy conversion between kinetic and potential is not ideal, there is always loss during each cycle. To quantify the efficiency of energy conversion, the quality factor(Q) is used to define the ratio of stored energy versus lost energy during one cycle of vibration. It can be defined as[6]:

$$Q = 2\pi \frac{peak \quad energy \quad stored}{energy \quad dissipated \quad per \quad cycle} \tag{2.5}$$

It can also be represented by energy loss mechanisms that occur in a resonator[47]:

$$\frac{1}{Q} = \frac{1}{Q_{medium}} + \frac{1}{Q_{clamping}} + \frac{1}{Q_{intrinsic}} + \frac{1}{Q_{other}} \tag{2.6}$$

where Q_{medium}, $Q_{clamping}$, $Q_{intrinsic}$, and Q_{other} are the quality factors associated with the interaction of mechanical structure with a medium, energy loss over the physical clamping, all dissipation mechanisms happening within the resonator, and other loss mechanisms.

Besides using the quality factor to describe the performance of the resonator, the effective electromechanical coupling coefficient ($k^2_{coupling}$) can also quantify the energy conversion efficiency. The effective electromechanical coupling coefficient can be expressed as[1]:

$$k^2_{coupling} = \frac{f_p^2 - f_s^2}{f_p^2} \tag{2.7}$$

where f_p and f_s are the resonance frequency and anti-resonance frequency. In figure 2.2, When a one-port piezoelectric resonator reaches its anti-resonance frequency, it exhibits minimum impedance, and when it reaches its resonance frequency, it shows maximum impedance.

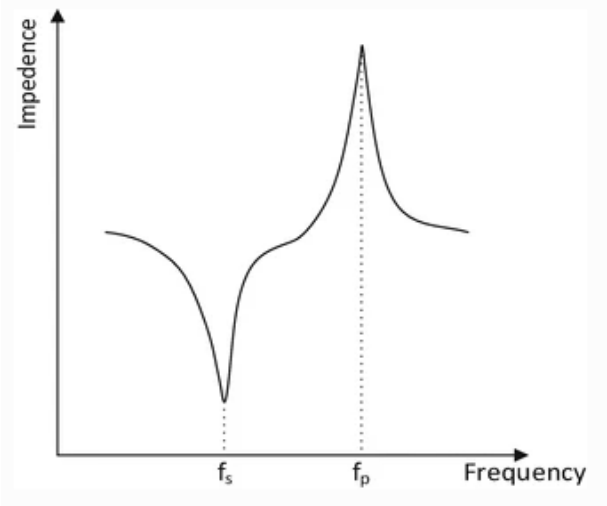

Figure 2.2: A typically measured impedance (magnitude) for a one-port piezoelectric resonator. Reprinted by[6]

2.2.2. Lumped element modeling of general MEMS resonator

Mechanical vibrations of a mass-spring-damper system are associated with the periodic conversion of kinetic energy and vice versa, and it is similar to the behavior of the MEMS Resonator in a linear regime. For a small vibration MEMS resonator, the basic resonator structure can be represented as a mass-spring-damper system, the figure is shown in figure 2.3. Using Newton's laws of motion, x is the displacement amplitude, m_{eff} is effective mass, b_{eff} is effective damping and k_{eff} is effective stiffness, the mass-spring-damper model can be expressed as follow[1]:

$$m_{eff}\frac{\partial^2 x}{\partial t^2} + b_{eff}\frac{\partial x}{\partial t} + k_{eff}x = F_{drive} \tag{2.8}$$

F_{drive} is the driving force of the MEMS system. The system transfer function can be obtained by rearranging and transforming to the Laplace domain, the transfer function can be obtained by:

$$H(s) = \frac{X(s)}{F_{drive}(s)} = \frac{1}{m_{eff}s^2 + b_{eff}s + k_{eff}} \tag{2.9}$$

and the quality factor from the above transfer function can be expressed as:

$$Q = \frac{1}{b_{eff}}\sqrt{m_{eff}k_{eff}} \tag{2.10}$$

An alternative way to model the dynamic behavior of MEMS resonators is by using a circuit model. From an energy point of view, the force (F) in the mechanical domain can be correlated with voltage(V)

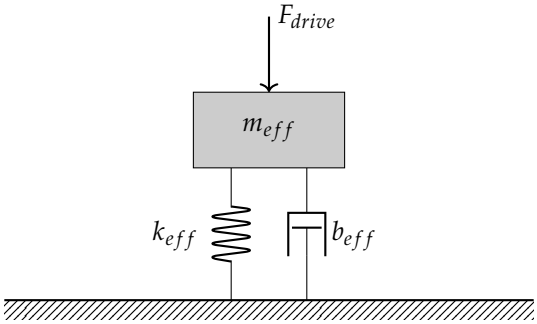

Figure 2.3: Mass-spring-damper model

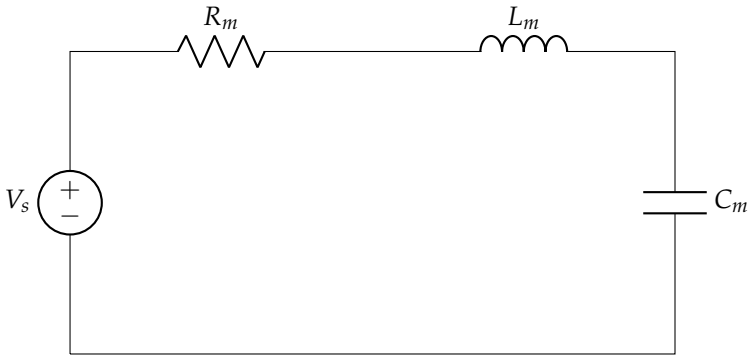

Figure 2.4: Equivalent circuit model

in the electric domain, velocity ($V_{velocity}$) can be linked to current (i), and displacement (x) can be related to the charge (q). Calculating the transfer function of the circuit model in the Laplace domain results in a similar equation:

$$H(s) = \frac{I(s)}{V(s)} = \frac{s}{L_m s^2 + R_m s + \frac{1}{C_m}} \tag{2.11}$$

where R_m is Resistor, L_m is inductor, and C_m is capacitor. The equivalent circuit model of the mass-spring-damper system is shown in figure 2.4. The quality factor can also be rewritten as:

$$Q_{eff} = \frac{1}{R_m}\sqrt{\frac{L_m}{C_m}} = \frac{f_p}{BW} \tag{2.12}$$

Where the f_p is resonance frequency and BW is the -3dB bandwidth.

2.2.3. BVD modeling of piezoelectric MEMS resonator

Circuit analogies permit efficient modeling of the interaction between the electronic and the non-electronic components of a microsystem. It can help optimize the system's overall performance. To model the performance of a thin-film piezoelectric MEMS resonator, the Butterworth Van Dyke (BVD) model is often used[28]. The BVD model consists of a motion branch, R_m, L_m, C_m in a series of RLC circuit, and a static branch with a static capacitance C_0. It is a one-port network and the figure is shown in 2.5. The effective electromechanical coupling coefficient of a piezoelectric resonator could be defined as

$$k^2_{coupling} = \frac{C_m}{C_0} \tag{2.13}$$

2.3. Ultrasound transducer

In medical ultrasound imaging applications, the ultrasound transducer serves as the heart of the system. Three primary categories of ultrasound transducers have been documented, namely bulk piezoelectric

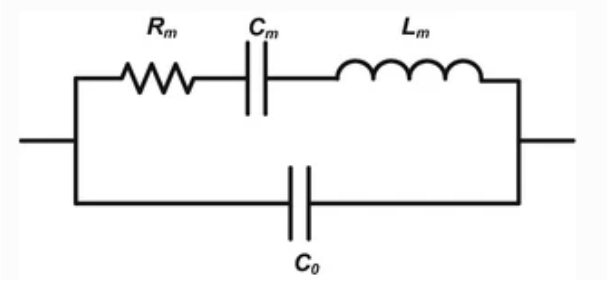

Figure 2.5: Basic BVD model of a piezoelectric resonator. Reprinted by[6]

transducers, capacitive micromachined ultrasound transducers (CMUT), and piezoelectric micromachined ultrasound transducers (PMUT)[44]. They can convert electrical energy into mechanical energy and vice versa, but the working principles of 3 ultrasound transducers are different.

Back in 1880, piezoelectricity was discovered in a single crystal. Piezoelectricity is the phenomenon where electric charge accumulates in piezoelectric materials in response to mechanical stress. For different piezoelectric materials, there are different piezoelectric coefficients (d_{ij}). In 1946, piezoelectric ceramics dominated the major ultrasound transducer industries[40]. In 2009, the production of ultrasonic transducer probes(mainly bulk piezoelectric transducers) amounts to a global market of about 1 billion dollars annually[24]. For now, this technology has matured considerably and remains in use for ultrasound imaging. Bulk piezoelectric transducers, also known as conventional piezoelectric transducers, typically have a three-layer structure consisting of a piezoelectric layer, a backing layer, and a matching layer[32]. The figure is shown in 2.6, the backing layer is used to give mechanical support to the transducer and dampen the echo to decrease the pulse duration and absorb some of the energy from the backward sound, and the matching layer is used to reduce the acoustic impedance mismatch between the piezoelectric layer and biological tissue to increase the energy transmission efficiency[32][37]. Taking advantage of the piezoelectric effect, the bulk ultrasound transducer can function in thickness mode (d33-mode). The first 3 in the subscript in d33 means that the voltage is generated along the z-axis, and the second 3 means that the direction of the applied force is also on the z-axis. In this mode, the frequency of transducers is determined by the thickness of the piezoelectric layer.

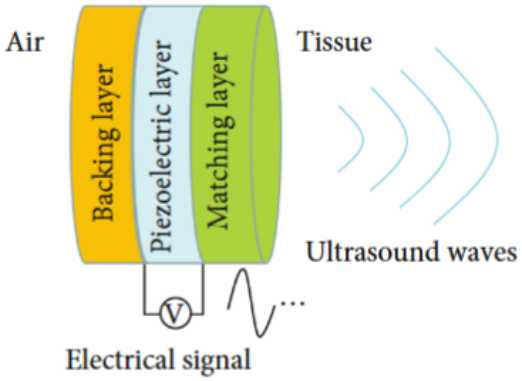

Figure 2.6: Bulk ultrasound transducer. Reprinted by[32]

However, as the microelectronics industry advances and the demand for portable ultrasound transducer probes and minimized devices grows, there is the active pursuit of micromachined ultrasonic transducers (MUT) in numerous research and industrial settings. MUTs are membrane structures with improved acoustic impedance matching with the load medium. Consequently, they do not require the matching layer[8]. With the development of microelectromechanical systems (MEMS) fabrication technology, the new technology enabled us to construct transducers, whether large or small, with highly intricate ge-

(a) Schematic of CMUT. Reprinted from[20]

(b) Schematic of PMUT. Reprinted from[8]

Figure 2.7: Schematic of MUT side view

ometries, and achieve this with great precision and cost-effectiveness, an accomplishment beyond the capability of bulk ultrasound transducer fabrication technologies[24]. Within the MUT category, there are Capacitive Micromachined Ultrasonic Transducers (CMUT) and Piezoelectric Micromachined Ultrasonic Transducers(PMUT). During the mid-1990s, the invention of CMUT occurred, and it entered the medical ultrasound market around 2010 [23]. The structures of CMUT are different, the main structure of CMUT is a capacitor cell with a fixed plate and a moveable thin flexible plate. The figure of CMUT is shown in 2.7a, it is based on the electrostatic actuation principle. When DC voltage is applied between two plates, it will cause a deflection of the thin flexible plate. When AC voltage is applied between two plates, it will cause a vibration of the thin flexible plate and generate ultrasound waves. For receiving the ultrasound waves, it needs to apply a biased voltage to the two plates, and it can detect the capacitance change based on the generated electrical current. The working frequency of CMUT depends on the shape, dimension, and mechanical property of the plates[23] [20].

PMUT was invented in 1983, and its initial application in imaging took place in 1997[45]. Compared with CMUT, the working principle of PMUT relies on the piezoelectric effect. Hence, PMUT operates without the need for high bias voltage, which, if present, would constrain its application in low-voltage electronics and pose potential risks for internal body applications. Compared with bulk ultrasound transducers, PMUT operates in the bending mode or flexural mode (d31 mode), distinguishing it from bulk piezoelectric transducers. The different structures with bulk ultrasound transducers enable PMUT to avoid the issues of poor acoustic impedance mismatch, and the new MEMS fabrication technology facilitates the miniaturization of PMUT at a more affordable cost. PMUT is a multi-layer structure, including a minimum of one piezoelectric layer sandwiched between two metal layers(electrode) and a base structural layer, and the figure of PMUT is shown in 2.7b. When an AC voltage is applied on the electrodes across the piezoelectric layer, the out-of-plane electric field generates in-plane stresses in the piezoelectric layer.[11] This way allows the PMUT to function as a transmitter, where the application of AC voltage induces vibration in the PMUT, resulting in the generation of an ultrasound wave. Benefiting the reverse piezoelectric effect, when the PMUT functions as a receiver, the application of an acoustic wave to the PMUT structure leads to the generation of voltage on the electrodes.

2.4. PMUT modeling

The general piezoelectric MEMS resonator modeling is presented in section 3, however, it is not enough to predict the behavior of the specific resonator. Specific Analytical modeling can predict device performance such as resonance frequency, and vibration amplitude, offering a method to analyze data and optimize designs. The following subsection will include an analytical model to derive the mode shape and resonance frequency of the first vibration mode of circular PMUT and an equivalent circuit model to predict the circular PMUT's dynamic behavior.

2.4.1. PMUT analytical model

Traditional PMUT is a multi-layer circular plate, and the structural response is based on the classical plate theory. For a planer laminate with N layers, the figure shown in 2.8, the location of the neutral

plane Z_s is calculated in [51].

$$Z_{NA} = \frac{\sum_{i=1}^{N} t_n Z_n Y'_{11,n}}{\sum_{i=1}^{N} t_n Y'_{11,n}} \tag{2.14}$$

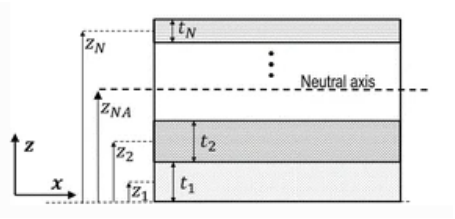

Figure 2.8: Laminate cross-section. Reprinted by[7]

where t_n is the thickness of the n-th layer, $Z_n = \sum_{i=1}^{n-1} t_i + \frac{1}{2}t_n$, and $Y'_{11,n} = \frac{Y_{11,n}}{1-\nu^2_{12,n}}$. And $Y_{11,n}, \nu_{12,n}$ represents the in-plane Young's moduli and in-plane Poisson ratio respectively.

Earlier studies have explored an analytical model for PMUT. In the case of a clamped circular PMUT, the most general form of the vibration equation or the governing equation is as follows[50] :

$$D\nabla^2\nabla^2\omega_N + I_0\frac{\partial^2\omega_N}{\partial^2 t} = \nabla^2 M_p + F_{ext} \tag{2.15}$$

where ω_N is the displacement, M_p is piezoelectric induced moment caused by the applied voltage, F_{ext} is applied external force, D is the flexural rigidity, I_0 is mass per unit area and equal to

$$I_0 = \sum_{i=1}^{q} \rho_i t_i \tag{2.16}$$

where ρ_i is the density of the i-th layer, and the flexural rigidity (D) is determined in [7],

$$D = \frac{1}{3}\sum_{n=1}^{N} Y'_{11,n}(\hat{h_n^3} - \hat{h_{n-1}^3}) \tag{2.17}$$

where $\hat{h_n} = h_n - Z_s$ is the distance from the top of the n-th layer to the neutral axis.

To simplify the calculation, only the homogeneous solution of the governing equation is taken into account, and any non-axisymmetric vibrations will be neglected. The mode shape function ($\phi_{ij}(\bar{r}, \theta)$) that delineates the deflection profile of a circular plate when no external moment or force is applied can be described as follows[50]:

$$\phi_{ij}(\bar{r}, \theta) = [J_i(\lambda_{ij}\bar{r}) - \frac{J_i(\lambda_{ij})}{I_i(\lambda_{ij})}I_i(\lambda_{ij}\bar{r}))]cos(j\theta) \tag{2.18}$$

where J_i, I_i are Bessel functions, $\bar{r}$ is normalized radius ($\bar{r} = \frac{r}{a}$, a is the radius of the plate) and the eigenvalues λ_{ij} are the solution of

$$J_i(\lambda)I_{i+1}(\lambda) + I_i(\lambda)J_{i+1}(\lambda) = 0 \tag{2.19}$$

Where the fundamental eigenvalues of circular plate $\lambda^2_{00} = 10.22$. For the first vibration mode, the mode shape is given by

$$\phi_{00}(\bar{r}) = [J_0(3.2\bar{r}) - 0.0555I_0(3.2\bar{r}))] \tag{2.20}$$

To simplify the following analysis, the simplified mode shape of the first vibration mode of a circular plate is given by:

$$\omega(\bar{r}) = (1 - \bar{r}^2)^2 \tag{2.21}$$

The eigenfrequency of the PMUT's fundamental vibration mode from equation 8 is

$$f_n = \frac{\lambda_{ij}}{a^2}\sqrt{\frac{D}{\mu}} \tag{2.22}$$

where $\mu = \sum_{n=1}^{N} t_n \rho_n$.

2.4.2. PMUT equivalent circuit

Equivalent circuit models serve as powerful tools in addressing multi-physics problems. In the context of PMUT, these models include the mechanical, electrical, and acoustic domains. An equivalent circuit model of the fundamental resonance mode is shown in figure 2.9.

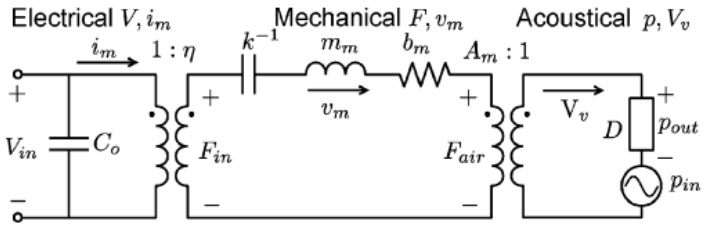

Figure 2.9: PMUT equivalent circuit. Reprinted from[43]

The mechanical lumped parameters can be calculated by using the displacement function $\omega_N(r)$. The average deflection will be used for the mechanical lumped parameter calculation.

$$\omega_{ave} = \int_0^a 2\pi r \omega_N(r)\, dr \tag{2.23}$$

The structural compliance C_m can be obtained by average deflection divided by the force due to the uniform pressure(p) on the PMUT[11].

$$k^{-1} = C_m = \frac{\omega_{ave}}{\pi a^2 p} = \frac{\int_0^a 2\pi r \omega(r)\, dr}{\pi a^2 p} \tag{2.24}$$

The equivalent mass is calculated by the total kinetic energy(E_K), velocity of the plate $u(r) = 2\pi f \times \omega(r)$ (f is frequency) and L_m is given by[11]:

$$E_k = \int_0^a u(r)^2\, dm = \frac{1}{2} m_m u_{avg}(r)^2 \tag{2.25}$$

$$m_m = L_m = \frac{\int_0^a u(r)^2\, dm}{u_{avg}(r)^2} = \frac{\int_0^a 2\pi\rho t \omega(r)^2\, dr}{(\int_0^a 2\pi r \omega(r)\, dr)^2} \tag{2.26}$$

The damping of the PMUT is mechanical resistance in the equivalent circuit, it can be calculated by using the quality factor(Q).

$$b_m = R_m = \frac{1}{Q}\sqrt{\frac{L_m}{C_m}} \tag{2.27}$$

In the acoustic domain, the acoustic impedance is given by [43],

$$D = \frac{\rho_a C_a}{A_m}\left(1 - \frac{J_1(2ka)}{ka} + j\frac{H_1(2ka)}{ka}\right), k_{number} = \frac{2\pi}{\lambda} \tag{2.28}$$

where ρ_a is the density of the acoustic material, λ is the wavelength of the sound, J_1 is first order Bessel function and H_1 is the first-order struve function, A_m is effective area of plate. The transformer in the equivalent circuit is ideal, the ratio of the transformer from the electrical domain to the mechanical domain can be expressed as [7]

$$\eta = \frac{1}{2} e_{31} (Z_n - Z_{NA}) I_p \tag{2.29}$$

The second transformer ratio from the mechanical domain to the acoustic domain, and can be estimated as[54]

$$A_m = \frac{1}{3} \pi a^2 \tag{2.30}$$

2.5. PMUT fabrication technology

PMUT is a multi-layered structure with different materials for each layer. It consists of a device layer, a buried layer, a bottom electrode, a thin piezoelectrical layer, and a top electrode. Besides the design and modeling of PMUT, a proper fabrication method is vital to reach the desired value. There are two general technologies for building the micromechanical structure of PMUT, which are bulk micromachining and surface micromachining.

Bulk micromachining technology defines structure by selective etching through the back side of the substrate or bulk material to form the desired structure[15]. For PMUT, use a deep etching method to release PMUT's membrane. In paper [3], authors fabricated their PMUT by bulk micromachining, the flow chart is reprinted in figure 2.10. The process includes the wet oxidation of silicon wafers, and oxide etch and silicon etch to release the silicon membrane. Followed by e-beam evaporation to form the bottom electrode, sol-gel processing to deposit the piezoelectric layer(PZT), and sputtering to deposit the top electrode. Finally, the top layer is patterned and etched to create a contact of the bottom electrode. The second PMUT fabrication work is similar [22], authors fabricated their PMUT with a double-sided polished si wafer and deposited ALN passive layer rather than the silicon dioxide. Then, the bottom electrode, the ALN active piezoelectric layer is patterned and deposited. Followed by depositing the top electrode and creating an open by a wet etch process. The final step is a deep reactive ion etch to release the membrane. Numerous similar procedures are involved in bulk micromachining technology for PMUT design, and these can be referenced in the existing literature[16],[31].

Surface micromachining technology requires the deposition of mechanical layers on the wafer and the selective removal of one or more sacrificial layers to form the desired structure[15]. In this technology, the membrane of PMUT is released from the surface. In paper [58], figure 2.11 shows the flow chart of this process. The PMUT fabrication process begins with the thermal oxidation of the silicon wafer and the subsequent deposition of amorphous silicon acts as a sacrificial layer. Then, applying sputtering to coat the sacrificial layer with ALN, followed by etching to create an opening for the release hole, facilitates the removal of the sacrificial layer. Subsequently, sputtering to deposit the ALN, bottom electrode, and top electrode. In the last step, the top layer is etched to open a vias to the bottom electrode. In paper [48], the author introduces a novel fabrication process. To release the membrane of PMUT, the array of holes is etched in the silicon wafer and annealed to form the membrane. Then, the silicon is doped to form the bottom electrode. After that, the piezoelectric layer and top electrode are patterned and deposited.

2.6. Figure of merit of PMUT

As an ultrasound transducer, PMUT is essential for obtaining clear and precise images of bodily tissues. To enhance image quality, certain parameters in PMUT design must be improved, such as axial resolution and image clarity. A higher bandwidth of PMUT is necessary to enhance axial resolution, while increased sensitivity is required to improve overall image clarity. Therefore, two important metrics for PMUT performance are the displacement sensitivity $d_s(f_n)$ and bandwidth, and it can be expressed as follow[59]:

$$d_s(f_n) = Q d_s(0) \tag{2.31}$$

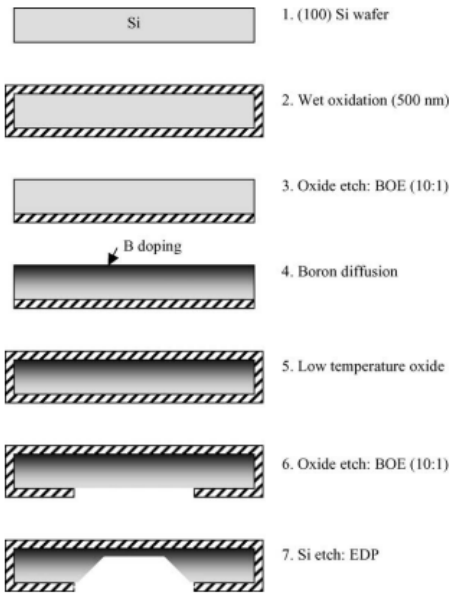

(a) Bulk micromachining flow chart 1

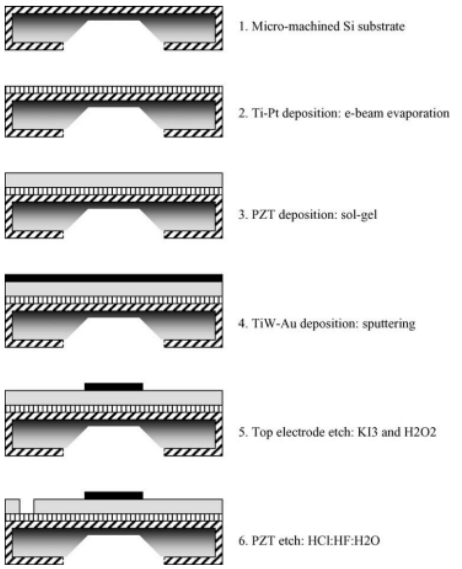

(b) Bulk micromachining flow chart 2

Figure 2.10: Bulk micromachining flow chart. Reprinted from[3]

$$d_s(0) = d_s(f_n)\frac{Bandwidth}{2\pi f_n} \tag{2.32}$$

$$d_s(0) = -a^2\frac{M_p I_p}{D I_d} \tag{2.33}$$

where $d_s(0)$ is the static displacement of PMUT(this parameter $d_s(0)$ refers to the highest displacement of the PMUT thin-film when the frequency is 0. The $\omega_N(r)$ refers to the displacement function of the film from the center to different positions), M_p is the piezoelectric moment, I_p is integrals related to the electrode layout and mode shape, and I_d is integrals related to the bending moment and model stiffness. Both I_p and I_d depend on the vibration mode shape[12].

$$M_P = e_{31,f}(Z_n - Z_{NA}) \tag{2.34}$$

$$I_p = \int_0^{r_{top}} (r\frac{d^2\omega(r)}{dr} + \frac{d\omega(r)}{dr})\, dr \tag{2.35}$$

$$I_d = \int_0^1 [(\frac{d^2\omega(r)}{dr} + \frac{1}{r}\frac{d\omega(r)}{dr})^2 - 2(1-v)\frac{1}{r}\frac{d\omega(r)}{dr}\frac{d^2\omega(r)}{d^2r}]r\, dr \tag{2.36}$$

However, from the equations above, it is readily apparent that enhancing displacement sensitivity results in a decrease in bandwidth, or vice versa. So, a figure of merit (sensitivity times bandwidth) of PMUT is essential. Consequently, timing the relationship between $d_s(f_n)$ and bandwidth can assist designers in making rough design decisions to achieve optimal design parameters. By considering the simplified mode shape and assuming the same material for each layer the sensitivity times bandwidth can be expressed as:

$$d_s(f_n) \times Bandwidth \propto \frac{e_{31,f}}{t^2}(Z_n - Z_{NA}) \tag{2.37}$$

For a two-layer simplified structure PMUT, with two negligible thickness electrodes a piezoelectric layer, and a substrate, it can be simplified as

$$d_s(f_n) \times Bandwidth \propto \frac{e_{31,f}}{t^2} t_1 \tag{2.38}$$

where t_1 is the thickness of the substrate. It shows the optimization of circular PMUT performance by geometry depends on the thickness of the entire PMUT and the distance between the top layer and the neutral axis.

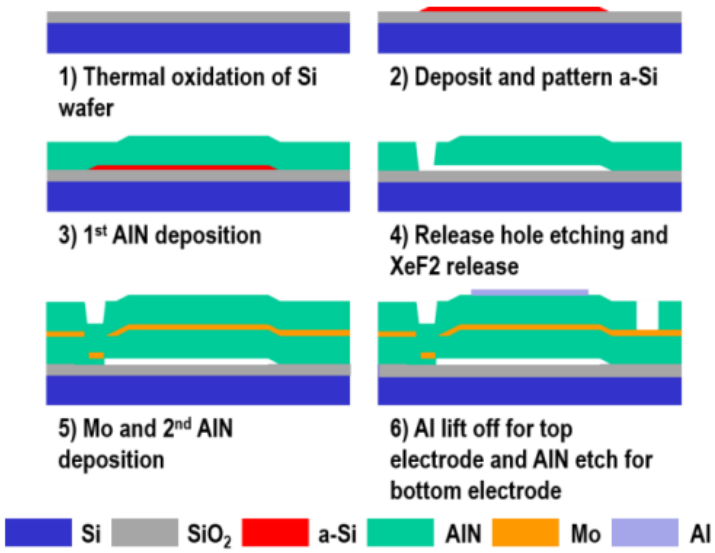

Figure 2.11: Surface micromachining flow chart. Reprinted from[58]

3

Quality factor and bandwidth control through PMUT structure design and electronic feedback

3.1. Broaden bandwidth through PMUT structure design

In ultrasound imaging applications, a shorter pulse length represents a better axial resolution of imaging. Hence, a method to attain a broad bandwidth for a single PMUT involves the optimization of its geometry structure. There are different shapes of PMUT to realize the wide bandwidth. In paper [60], the author designs a PMUT with a rectangular membrane to overcome the bandwidth limitation(figure 3.2). The resonance frequency of rectangular-shaped membranes can be designed to be very close together when the length (L_x) and width (L_y) aspect ratio (k) are large. The first and third modes are merged to reach the wide bandwidth. (The measured -6dB bandwidth is 95% in water.) Based on the modal frequency from [60],

$$f_{m,1} = \frac{1}{2L_y}\sqrt{\frac{T}{\rho}}\sqrt{\frac{1}{k^2}+1} \times \sqrt{\frac{m^2+k^2}{k^2+1}} \tag{3.1}$$

where T is the surface tension, and ρ is the area density. The first part of the equation $\frac{1}{2L_y}\sqrt{\frac{T}{\rho}}\sqrt{\frac{1}{k^2}+1}$ is the fundamental frequency. The rest part will reduce the distance from the m mode to the fundamental mode by increasing the length/width ratio k. However, in the air-coupled scenario, the PMUT needs to apply DC (Direct current) biasing to merge the resonance modes. For ferroelectric materials such as PZT, the application of a DC bias results in the polarization of the thin membrane, leading to a decrease in the dielectric constant and a subsequent reduction in the piezoelectric coefficient[27]. In the case of non-ferroelectric materials like ALN, applying a DC bias can still enhance the bandwidth of PMUT. However, this enhancement is achieved by increasing anchor loss, resulting in a decrease in the quality factor and an increase in bandwidth[64].

Another design from [13] finds a method to broaden the bandwidth of a single PMUT by using the ring-shaped structure PMUT(Figure 3.2a). The structure includes an annular electrode on the top and a rigid center post in the cavity to mechanically fix the middle region. The ring-shaped PMUT can have a high bandwidth when the PMUT is working in a liquid environment. The working principle is different with rectangular PMUT, the wide bandwidth generated by rectangular PMUT is based on the combination of its resonance mode. The ring-shaped PMUT depends on the merging of the first resonance mode and acoustic-induced second resonance. In the equivalent circuit modal of PMUT, the second resonance mode is caused by the acoustic impedance. When the acoustic impedance is minimized and the imaginary component of the mechanical-acoustic impedance is zero, the second acoustic-induced resonance and the fundamental resonance mode can occur. Due to the two close resonance modes, the

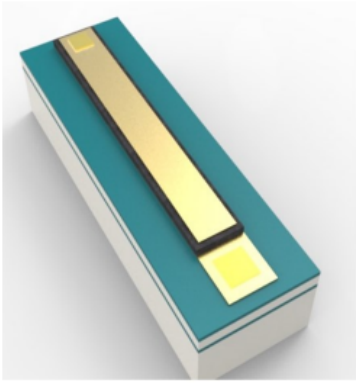

(a) Schematic of rectangular PMUT. Reprinted from[60]

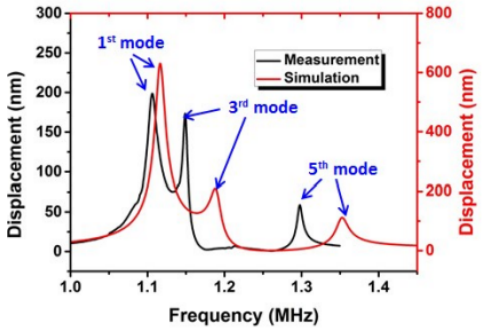

(b) Measured and simulated frequency response under 1 Vpp electrical excitation. Reprinted from[60]

Figure 3.1: Schematic of rectangular PMUT with measured and simulated results

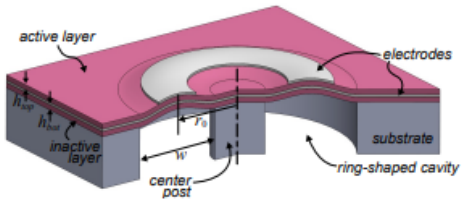

(a) Cross-sectional schematic of the (deformed) ring-shaped pMUT. Reprinted from[13]

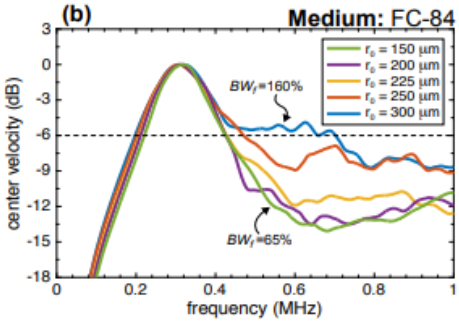

(b) Measured frequency response of ring-shaped PMUTs in FC-84. Reprinted from[13]

Figure 3.2: Schematic of ring-shape PMUT with measured results

bandwidth of the ring-shaped PMUT can broaden the bandwidth(Figure 3.2b).

Besides taking advantage of resonance modes merging to reach the wide bandwidth of PMUT, there is another method by using a Polydimethylsiloxane (PDMS) backing layer. In the paper [61], the author conducted a comparison between a circular PMUT with an empty cavity and a circular PMUT with a cavity filled with PDMS material(Figure 3.3). Due to the characteristics of PDMS material, PDMS can work as a load to PMUT without inducing a change in the working mode from flexural mode to thickness mode. The results indicate that the circular PMUT with a PDMS backing layer exhibits a broader -3dB bandwidth compared to the configuration without the PDMS backing layer. The reason for this phenomenon is that a structure with a backing layer tends to have an increased effective mass and higher effective damping, leading to a reduction in the quality factor of the PMUT. A reduced quality factor will increase the bandwidth of the PMUT.

PMUTS have been structurally modified to improve the bandwidth or sensitivity. In the following comparisons in table 3.1, varying displacement sensitivity in air and fractional bandwidth are presented, reflecting the impact of diverse structural designs. The fractional bandwidth is determined by dividing the bandwidth by the central frequency and the measurement results were generated in different environments. While various PMUT designs enhance bandwidth or quality factor, these parameters remain fixed and are unable to meet diverse requirements for ultrasound imaging, such as penetration depth and image clarity in different organs. In the next section, a new method will be introduced to control the bandwidth and quality factor in real-time.

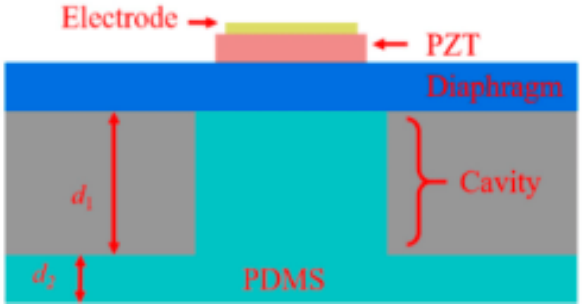

Figure 3.3: PMUT with PDMS backing layer. Reprinted by[61]

PMUT geometry	piezoelectric material	resonance frequency	displacement sensitivity	-6dB bandwidth	cite
Rectangular shape	PZT	1.24MHz	/	94.7%(water)	[60]
Rectangular shape	PZT	3.7 MHz	500nm/V(DC bias)	97%(Fluorinert FC-70)	[34]
Ring shape	ALN	320KHz	/	160%(FC-84)	[13]
Circular	PZT	8MHz	40 nm/V	62.5%(water)	[9]
Circular	ALN	25 MHz	2.5 nm/V	26%((Fluorinert-70)	[35]
Circular(with PDMS backing layer)	PZT	19.4MHz	33.2nm(displacement)	63%(water) @-3dB	[62]
Dome shape	PZNT	5Mhz	85 kPa/V(pressure)	55%(water) @-3dB	[17]
Square shape	ALN	400KHz	120 nm/V	/	[33]

Table 3.1: PMUT performance with different structure

3.2. Control bandwidth through electronic feedback

The performance of a system relies significantly on the bandwidth and quality factor of a MEMS resonator. The quality factor defines the ratio between stored energy and dissipated energy per cycle [26]. It has a strong impact on the sensitivity of the MEMS system. Instead of designing a specific structure to achieve a desired quality factor, it has been demonstrated that it is also possible to employ electronic feedback to control it [38]. This external electronic feedback method allows designers to introduce or extract energy from the system, thereby increasing or decreasing the quality factor and bandwidth.

For a small vibration MEMS resonator with external force, the fundamental resonator structure, the mass-spring-damper model can be expressed as follow[1]:

$$m_{eff}\frac{\partial^2 x}{\partial t^2} + b_{eff}\frac{\partial x}{\partial t} + k_{eff}x = F_{drive} \pm F_{ext} \tag{3.2}$$

F_{drive} is the driving force of the MEMS system, F_{ext} is the external force of the MEMS system. For the application of electronic feedback, the external 'force' can be the feedback current. In the process of external feedback, the motion of the resonator is converted into an electrical signal, and this electrical signal is proportional to the velocity. It can introduce positive or negative feedback. And the F_{ext} can be expressed as $F_{ext}(s) = b_{feed}s$ in the Laplace domain. Therefore, the ideal transfer function can be expressed as

$$H(s) = \frac{X(s)}{F_{drive}(s)} = \frac{1}{m_{eff}s^2 + (b_{eff} \pm b_{feed})s + k_{eff}} \tag{3.3}$$

and the new quality factor can be derived as:

$$Q_{eff} = \frac{1}{b_{eff} \pm b_{feed}}\sqrt{m_{eff}k_{eff}} \tag{3.4}$$

In the equivalent circuit model, b_{eff} equals to the R_m, m_{eff} equals to the L_m and k_{eff} equals to the $\frac{1}{C_m}$. The artificially modified quality factor will use the term "effective quality factor" to distinguish the origin definition of the quality factor of a resonator[36]. Therefore, the effective quality factor can be rewritten as:

$$Q_{eff} = \frac{1}{R_m \pm R_{feed}}\sqrt{\frac{L_m}{C_m}} \tag{3.5}$$

3.2.1. Positive/Negative feedback loop

A feedback loop system, whether positive or negative, entails the adding or deduction of a portion of the output value into the input. The relative block diagram can be found in the figure 3.4. When a positive (negative) feedback loop is implemented on a PMUT, the device needs to convert the resonator motion into an electrical signal proportional to the velocity and then provide feedback to drive the device[26]. This method of external velocity-proportional feedback control provides flexibility in addressing various scenarios. Users can opt to enhance sensitivity by increasing the quality factor or broaden the bandwidth by reducing the quality factor.

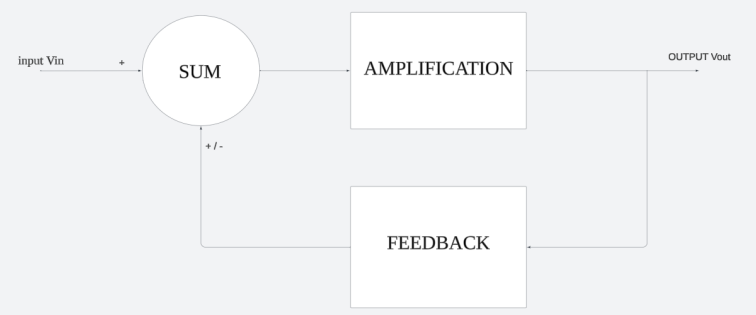

Figure 3.4: General block diagram of positive/negative feedback loop

In a fully realized circuit, an adder is commonly employed to receive both the input and feedback signals. As the current flows through the MEMS resonator, a compensation circuit becomes important to eliminate non-resonance current. Following this, a current-to-voltage conversion is essential to transform the current signal into voltage for feedback to the system. This ensures the voltage(force) signal in the feedback is proportional to the current(velocity). When different feedback specifications are required, an inverter facilitates the transition between negative and positive feedback, or vice versa. By appropriately selecting the resistance, control over the quality factor can be achieved. The relative block diagram in figure 3.5 and a positive feedback circuit can be found in 3.6. OP1 represents the function of an adder and OP3 works as a compensation circuit, and OP2 is an I-V converter. For the negative feedback loop, an inverter is needed to change the sign of the feedback signal.

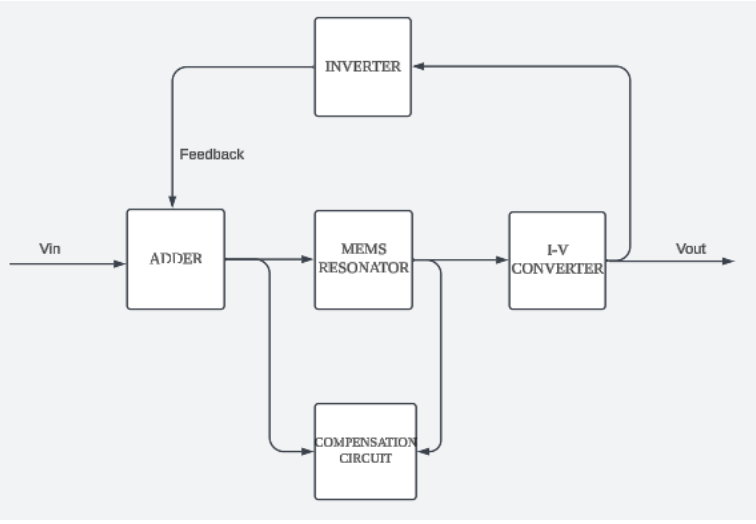

Figure 3.5: Circuit block diagram

3.2.2. Compensation for parasitic capacitance

In the MEMS resonator, the equivalent circuit model will consist of motional elements R_m, C_m, L_m, static capacitance C_0, and parasitic capacitance C_p. Due to the electronic configuration, when employing the electronic feedback method, the current flowing through the motional elements, static element,

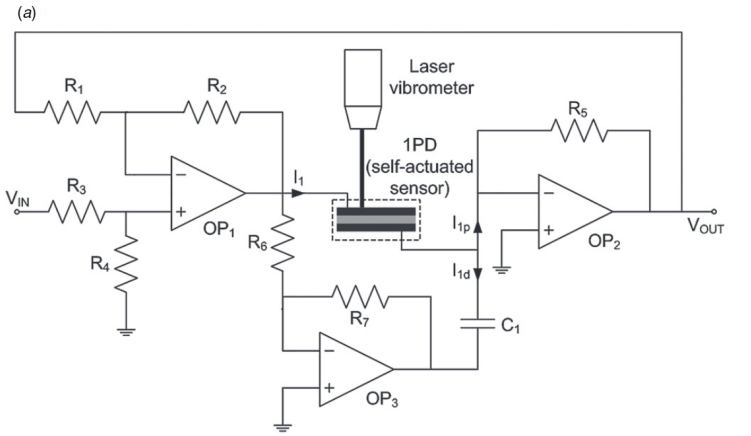

Figure 3.6: Positive feedback circuit. Reprinted from[26]

and parasitic element is fed back into the system. It will cause the resonator oscillation frequency to shift because of the unwanted signal[14]. It is necessary to eliminate the current passing through the static element and parasitic element. In this subsection, two methods of compensation will be introduced.

The first method is using the electronic circuit to cancel the parallel capacitance. The lower part circuit (Operational amplifier OP3 with resistors R_6 and R_7, and capacitor C_1 in figure 3.6)is used to create the compensation current which can "extract" the current from the parallel branches or the negative element in parallel with the resonator[14]. This approach requires precise measurements of the elements on the branch so that the cancellation circuit can utilize these values. The second method uses the dummy structure to compensate the unwanted branch [25]. The author uses a fully differential amplifier to drive the target and the dummy structure. The dummy structure has the same parasitic element and static element. The dummy structure receives a reversed driving voltage, which is provided by the second output of the fully differential amplifier. In this way, the dummy structure will create a 180°phase shift current to eliminate the branch current.

3.2.3. The limitation of quality factor control

The external electronic feedback loop method is powerful in tuning the quality factor, however, there is a limitation to this method. When a positive feedback loop is implemented, the effective quality factor will increase as the value of R_{feed} and R_m come closer. And the effective quality factor will reach the limit when the R_m is equal to the R_{feed}. The transfer function will be infinite and oscillations because the denominator in the formula (44) approaches zero[26]. Upon implementing a negative feedback loop, the constraint is determined by the overall circuit noise, with the noise generated from the MEMS resonator(PMUT) being negligible in comparison to that from the external circuit[55].

4

Commercial PMUT characterization test

4.1. Commercial PMUT electrical characterization test

This project will utilize commercial PMUTs manufactured and supplied by Silterra to demonstrate the use of electronic feedback in controlling the bandwidth or quality factor. The PMUT has been fabricated in a circular shape and the piezoelectric layer is sandwiched between two electrodes. The Piezoelectric layer's material is ALScN (9.5 %) with a thickness of 1.3 um. And the cavity diameter is 80 um. The cross-section and top view of PMUT are shown in figure 4.1.

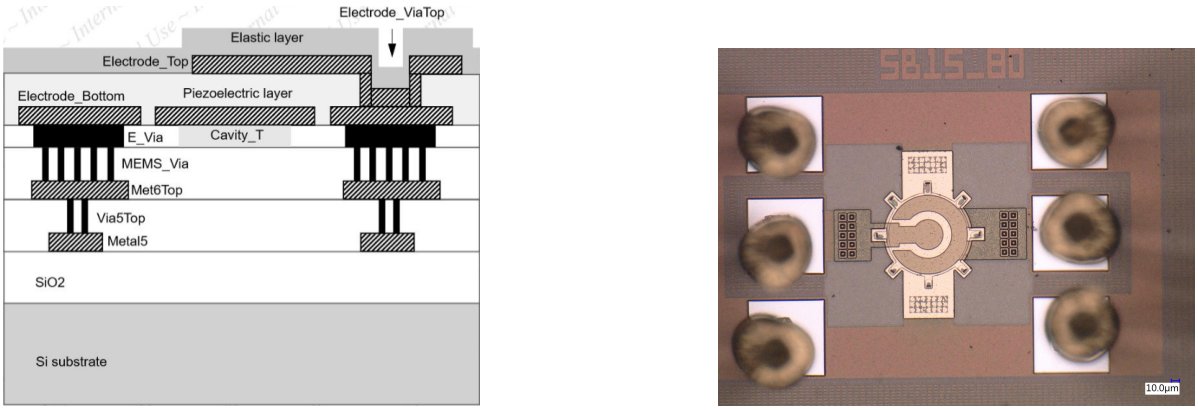

(a) Cross section of Commerical PMUT manufactured and supplied by Silterra

(b) Optical image of Commerical PMUT manufactured and supplied by Silterra

Figure 4.1: Cross section and optical image of PMUT manufactured and supplied by Silterra

To fully characterize the PMUT device, three general steps are followed. The first step is electrical characterization, where a probe station is used to measure and select the functional device. The probe station is equipped with probe arms and a vector network analyzer(VNA) for conducting the measurements. In the second step, a VNA or impedance analyzer is employed to verify the device's functionality after wire bonding and to fit the obtained data into an equivalent circuit model. Finally, the third step entails air-based PMUT measurement, which confirms the device's ability to generate an electrical signal in response to acoustic actuation.

4.1.1. PMUT in air electrical measurement

In this first electrical measurement, PMUTs will be glued on the silicon wafer using GE varnish, shown in figure 4.2a. The purpose of this measurement is to choose the functioning PMUT. The measurement uses a probe station and a vector network analyzer. The probe station includes 2 probe arms with

microprobe(from cascade Microtech) and the Vector network analyzer, KEYSIGHT P9374A, shown in figure 4.2b. After the measurements, two functioning PMUTs will be used for further measurements.

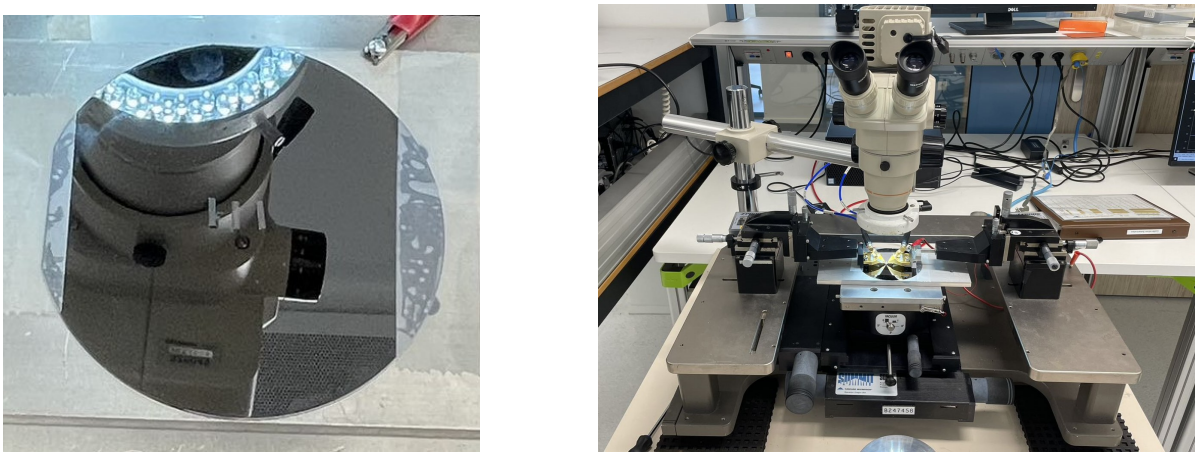

(a) Three PMUTs glued on wafer

(b) PMUT with probe station measurement

Figure 4.2: Measurement of commercial PMUTs using a probe station

After selections, PMUTs will be wire-bonding to the printed circuit board (PCB). The corresponding PCB design can be found in the figure C.2. The commercial PMUT has a two-port resonator structure, which can be modeled as the mass-spring-damper system. The motional resistance(Rm), motional inductance(Lm), and motional capacitor(Cm) determine the bandwidth or quality factor of PMUT device. Only by knowing these parameters, the circuit can be designed to change the effective motional resistance(Rm). Because the PMUT will be wire-bonded to the PCB and connected to the circuit for testing, the electrical characteristics of the PMUT need to be characterized after wire bonding to the PCB. Based on the parasitic capacitance, resistance, and inductance on the PCB, an equivalent circuit model of the PMUT on the PCB needs to be established to fit the data obtained under the electrical characteristics test. The equivalent circuit model of two port PMUT is shown in figure 4.3. Ls1 and Rs1 represent the inductance and resistance on the PCB trace. For the parasitic capacitance of the PCB, it is defined by the series resistance Rsp , the parallel resistance(Rp), and capacitance(Cp).

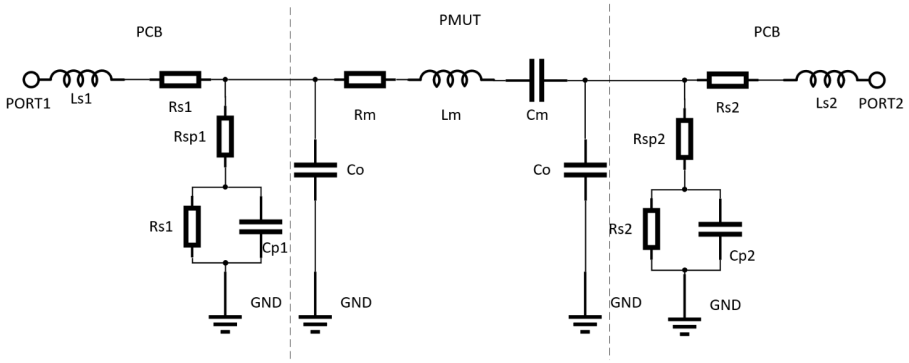

Figure 4.3: Equivalent circuit model of two port PMUT on PCB

The second electrical measurement is done by using an impedance analyzer and vector analyzer. In the impedance analyzer measurement, the PMUT will be considered a one-port device. However, the previously presented model (Figure 4.3) represents a two-port equivalent circuit. Therefore, to enable more accurate data fitting, the equivalent circuit of the PMUT with the PCB must be modified. To improve the accuracy of the fitting, Co will be ignored, as the Co of the commercial PMUT is in the femtofarad range, while the parasitic capacitance of the PCB is in the picofarad range. It is easy to

notice that the parasitic capacitance of PMUT in PCB will greatly influence the device's behavior and determine the anti-resonance frequency in one port measurement. The resulting modified equivalent circuit is shown in Figure 4.4. Due to the difference in parasitic capacitance on both sides and the two-port PMUT structure does not perfectly match, the results of the two ports will be slightly different. The results of the fitting are shown in figure 4.5, and the red line represents the measured data and the blue line represents the fitting curve. Table 4.1 shows the fitting data. However, for another PMUT the resonance from one port measurement is not obvious, the electrical measurement will be carried out by using a vector analyzer.

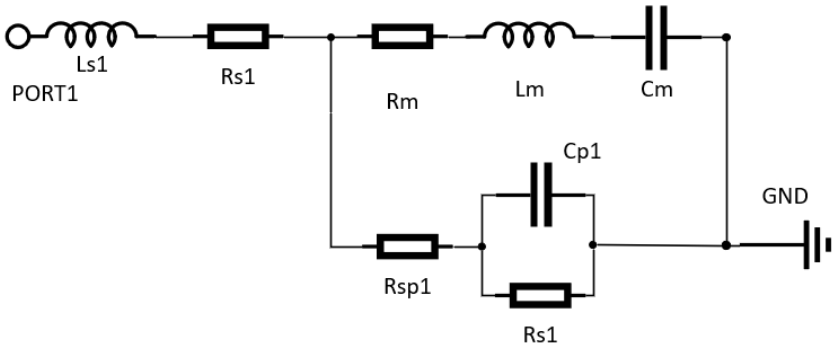

Figure 4.4: Equivalent circuit model of a one-port PMUT for function fitting

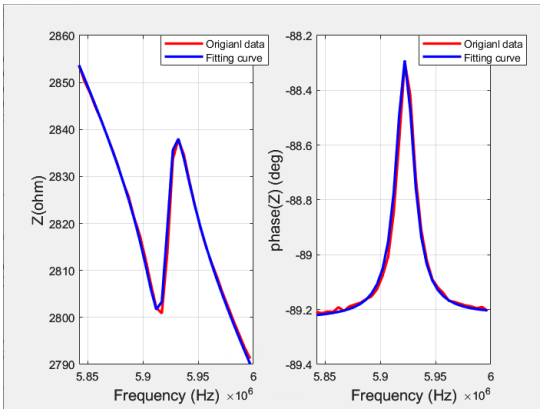

(a) Fitting result of Commerical PMUT in port one

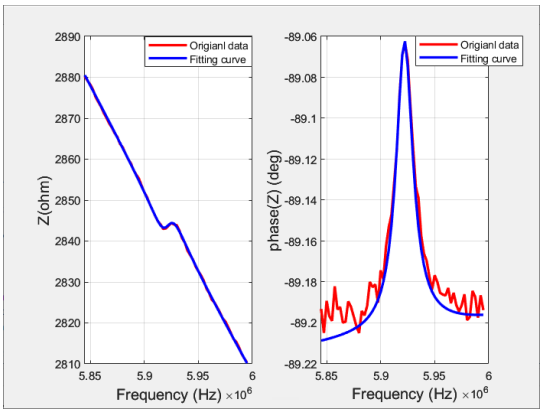

(b) Fitting result of Commerical PMUT in port two

Figure 4.5: Fitting result of commerical PMUT by impedance analyzer(The blue curve represents the fitted data, while the red curve represents the original data.)

	Rm(ohm)	Lm(H)	Cm(F)	Ls(H)	Rp(ohm)	Rsp(ohm)	Rs(ohm)	Cp(F)
Port1	1.7564e5	1.4143	5.1242e-16	6.4573e-7	1e6	30	4.4409e-14	9.45e-12
Port2	1.1454e6	9.6839	7.4825e-17	7.3144e-9	1e6	31.4	3.857e-14	9.7e-12

Table 4.1: Impedance analyzer fitting results of corresponding parameters

During vector network analyzer(VNA) measurement (KEYSIGHT P9374A), the PMUT will be treated as a two-port device. For the Y12 measurement, the voltage applied to port one is set to zero, allowing the device to measure the current flowing from the PMUT's motional branch at port two. This configuration helps eliminate the effects of parasitic capacitance. Therefore, the equivalent circuit model of the PMUT used for function fitting needs to be adjusted and it is shown in figure 4.6a. However, during the VNA measurement, the PMUT shows an anti-resonance frequency before the resonance frequency, which may be due to the multi-resonance mode of PMUT and the lower resonance frequency (lower than 5.9Mhz) causing this issue. The equivalent circuit model of the PMUT is shown in figure 4.6b. The fitting results of $PMUT_1$ and $PMUT_2$ can be found in figure 4.7 and 4.8 separately where the red

line represents the measured data and the blue line represents the fitting curve. Table 4.2 shows the fitting data of Rm, Lm, and Cm of the higher resonance frequency, and the lower resonance frequency Rm_s, Lm_s, Cm_s. And the parasitic capacitance (Cp) of $PMUT_1$ and $PMUT_2$ is around 10pf, based on the fitting results of the one port measurement.

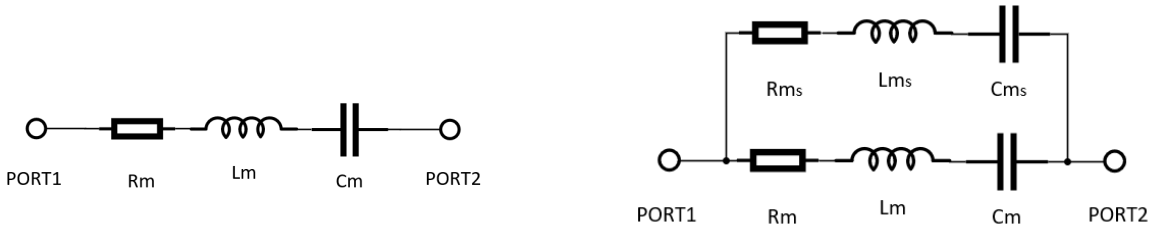

(a) General equivalent circuit single-mode model of a two-port PMUT for function fitting

(b) Equivalent circuit multi-mode model of a two-port PMUT for function fitting

Figure 4.6: Equivalent circuit models of a two-port PMUT for function fitting

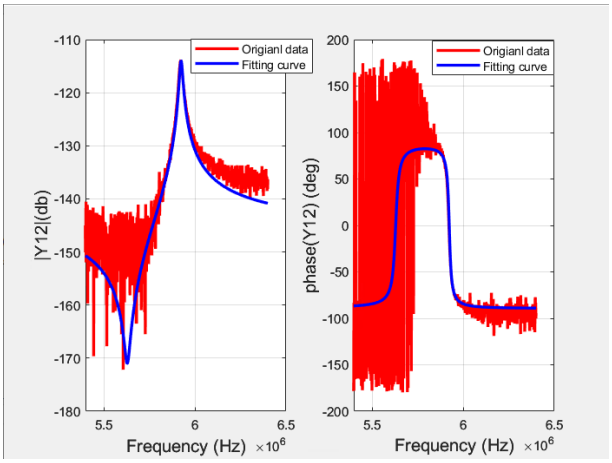

Figure 4.7: Fitting result of Commerical $PMUT_1$ by VNA (The blue curve represents the fitted data, while the red curve represents the original data.)

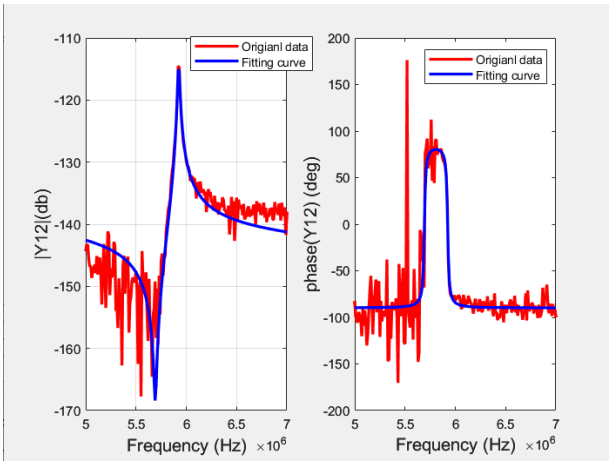

Figure 4.8: Fitting result of Commerical $PMUT_2$ by VNA (The blue curve represents the fitted data, while the red curve represents the original data.)

	Rm ohm	Lm(H)	Cm(F)	Rm_s(ohm)	Lm_s(ohm)	Cm_s(F)	Q
$PMUT_1$(Y12)	5.09e5	1.4143	1.3021e-16	6.1031e5	0.592	0.0344	204
$PMUT_2$(Y12)	5.29e5	4.0218	1.788e-16	1.168e5	0.1340	0.0267	283

Table 4.2: Fitting results of corresponding parameters of $PMUT_1$ and $PMUT_2$ by VNA

4.1.2. PMUT in liquid electrical characterization

Due to poor acoustic testing results in the air, the performance testing of the PMUT will be conducted in Isopropyl alcohol (IPA). In liquid, the attenuation of sound waves is smaller compared to air, and acoustic coupling is greater. However, before conducting similar testing, the electrical properties of the PMUT need to be re-characterized to determine the equivalent resistance. After testing with the VNA, the resonance point could not be read from Y12, as shown in the figure below. This is because when the liquid acts on the surface of the PMUT, it effectively applies pressure, increasing the equivalent resistance. In these two PMUTs, the equivalent resistance became too large, significantly reducing the quality factor, which resulted in the inability to read the resonance point,as shown in figure 4.9. Therefore, the upcoming PMUT tests in liquid cannot proceed.

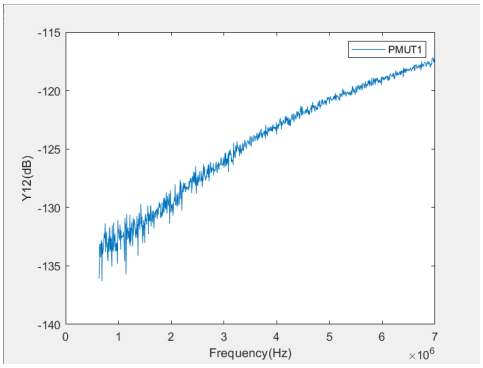

(a) $PMUT_1$ in IPA Y12 measurement without resonance by VNA

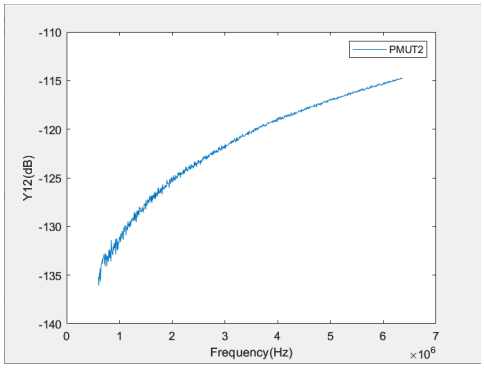

(b) $PMUT_2$ in IPA Y12 measurement without resonance by VNA

Figure 4.9: PMUT test in the IPA with VNA

4.2. PMUT in air acoustic actuation test

Ideally, an ultrasonic transducer(PMUT) should produce an electrical signal correlated to the ultrasound waves reaching its surface. However, the attenuation of the received ultrasound waves, and weak acoustic coupling will cause the electrical signal not detectable. To understand the functional capabilities of this PMUT, after the electrical characterization of the PMUT in the air, in-air measurement tests are required to verify that the PMUT can generate the piezoelectric current from the acoustic actuation.

After the verification, the PMUT can be utilized in a circuit to illustrate the concept of controlling bandwidth/quality factor. Figure 4.10 describes the test setup of the PMUT test in air to verify the PMUT can generate the piezoelectric current. In the figure 4.10a, PMUT is represented by a simplified equivalent circuit model of a two-port PMUT on a PCB. It is being acoustically actuated by a 5MHz ultrasound transducer (Panametrics V309). The current generated will be amplified by the low-impedance voltage amplifier (DHPVA-201) and read by the oscilloscope. In the figure 4.10b, the blue block is a function generator (Keysight EDU33212A), which generates the test signal for the ultrasound transducer in the yellow block. Based on the schematic, the generated current will flow through the voltage amplifier in the green block and will be displayed on the oscilloscope (Tektronix TBS 2000s).

During the in-air test, the $PMUT_1$ with 204 quality factor received 5.92Mhz, 10Vpp sin wave with 300 cycles, when the transducer was close to the center of PMUT with a distance around 0.2 μm. The result is shown in figure 4.11, the generated sin wave matches with the input sine wave signal from the ultrasound transducer. The attenuation of the received ultrasound wave has less influence

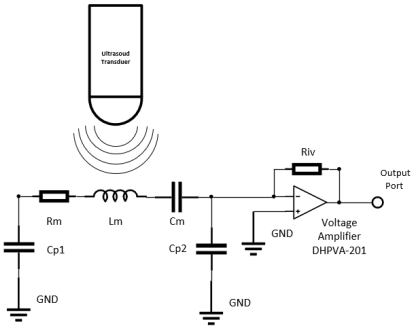

(a) PMUT in air acoustic actuation measurement schematic

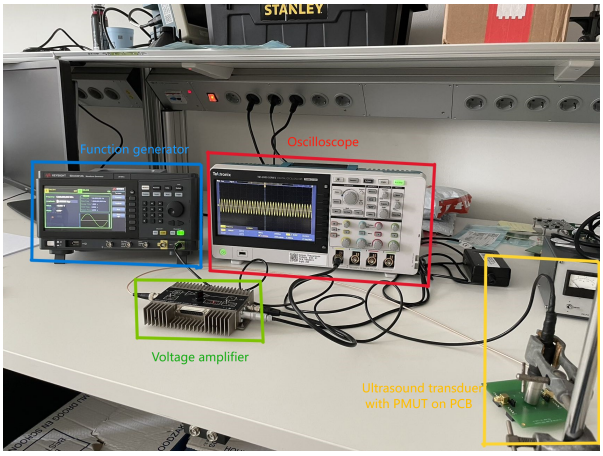

(b) PMUT in air acoustic actuation measurement picture

Figure 4.10: Test setup for PMUT in air acoustic actuation by ultrasound transducer measurement

on the generated signal, as indicated by the amplitude of the received voltage. However, based on the measurement results, the generated voltage from $PMUT_1$ does not exhibit the 'ring up' and 'ring down' phenomenon, which could mean that the acoustic signal from the ultrasound transducer is smaller than the electrical signal from the electrical coupling. This electrical coupling is caused by the pad of PMUT and the metal of the 5MHz ultrasound transducer, which forms a small capacitor and allows the electrical signal from the function generator to leak to the PMUT.

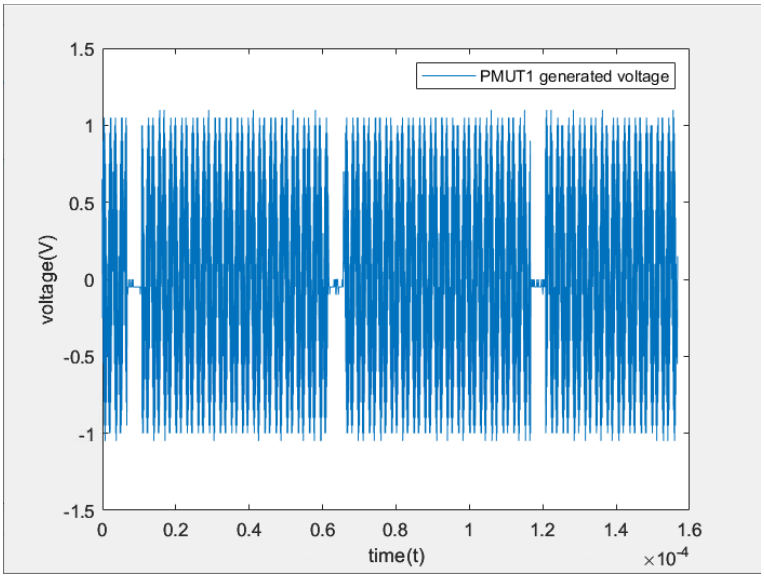

Figure 4.11: Generated output voltage after amplification from $PMUT_1$ in air acoustic actuation by ultrasound transducer measurement

Unfortunately, during the measurement, $PMUT_1$ was damaged and was not functioning properly. However, from the limited measurements, it appears the unwanted electrical coupling could have a large influence on the behavior of the PMUT output. Another PMUT will be tested in the air to verify whether it can generate the desired electrical signal. Two tests have been conducted to verify the idea. First, the test will be carried out with the ultrasound transducer has a fixed vertical distance with $PMUT_2$, but the ultrasound transducer will be placed above at the center of $PMUT_2$ or above the trace close to the output. In figure 4.12 and 4.13, the left figure is placement and the figure is measurement results. The blue curve represents the input voltage applied on ultrasound transducer, and the yellow

curve represents the generated output voltage after amplification from $PMUT_2$ in air acoustic actuation measurement. Both results indicate that $PMUT_2$ performs even worse in air actuation.

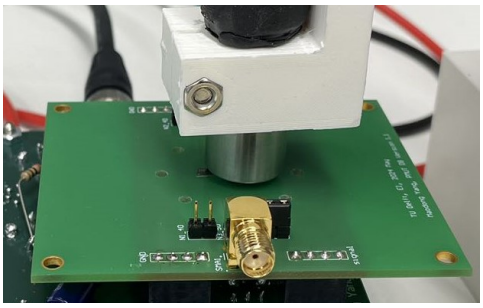

(a) Ultrasound transducer is placed in center

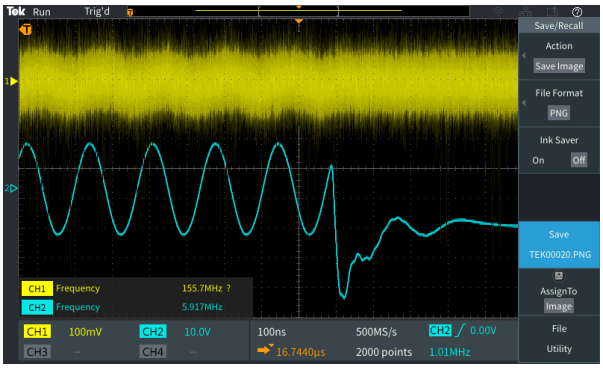

(b) Center placement test results

Figure 4.12: $PMUT_2$ test in the air with the center placement of ultrasound transducer (The blue curve represents the input voltage applied on ultrasound transducer, while the yellow curve represents the generated output voltage after amplification from $PMUT_2$ in air acoustic actuation measurement)

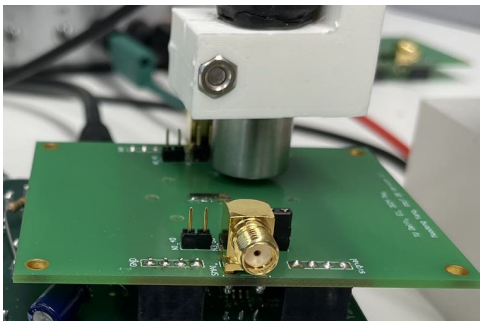

(a) Ultrasound transducer is placed closer to the output

(b) Deviate from center placement test results

Figure 4.13: $PMUT_2$ test in the air with deviation from center placement of ultrasound transducer (The blue curve represents the input voltage applied on ultrasound transducer, while the yellow curve represents the generated output voltage after amplification from $PMUT_2$ in air acoustic actuation measurement)

5

Quality factor modified circuit design and characterization

To fully achieve the function of quality factor control, the circuit in figure 5.1 has been applied. In this configuration, when the ultrasound transducer is excited with sound waves at the resonance frequency of the PMUT, the device generates the piezoelectric current. This current is converted to an output voltage via a current-to-voltage converter (OP2) and the resistor R_{iv}. The generated current is fed back to either increase or decrease the quality factor of the device. However, the electrical coupling affects the current generated, as observed in prior PMUT air tests. To validate the concept of using electronic feedback to control the PMUT's quality factor, a driving voltage is applied to the circuit, demonstrating the feasibility of this approach.

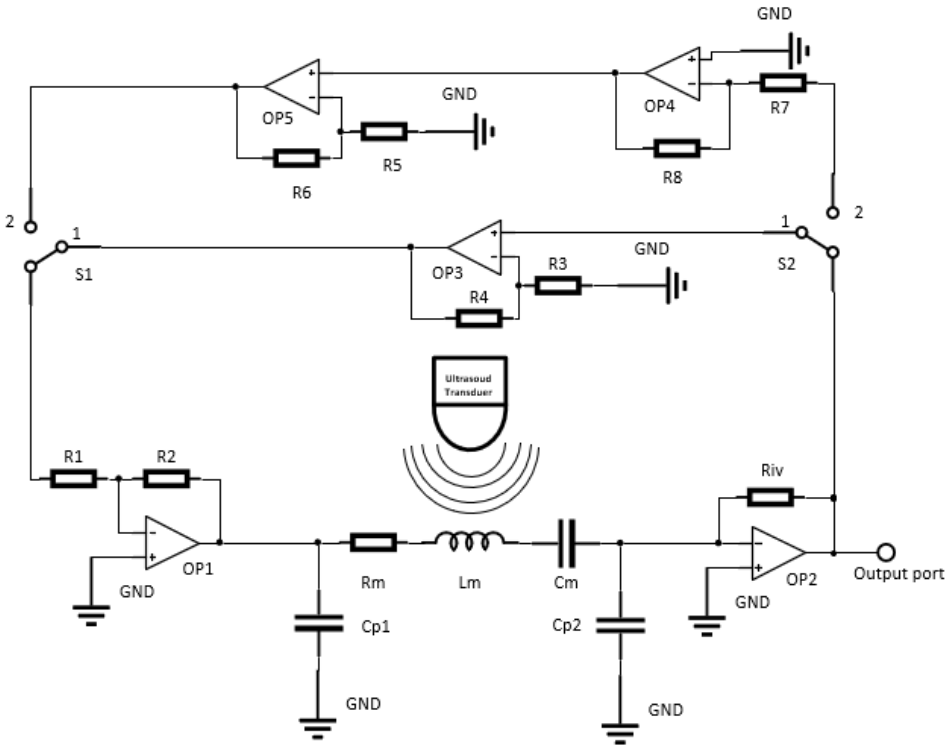

Figure 5.1: Increasing Q /Bandwidth circuit with acoustic actuation by ultrasound transducer

5.1. Quality factor increasing circuit

Due to the poor behavior of the PMUT in the air acoustic actuation test, the circuit needs to be modified. The driving voltage is connected with a Resistor(Rin) which has the same resistance as R1, and is applied to the input of operational amplifier OP1, which is responsible for electrically actuating the PMUT. In figure 5.2, the modified circuit is depicted. In the following circuit analysis, all operational amplifiers will be considered as ideal components. When Switch 1 (S1) and Switch 2 (S2) are set to port 1, the circuit functions as a quality factor enhancement circuit through the use of a positive feedback loop. OP1, operating as a summing amplifier, receives and amplifies both the driving waveform and the feedback signal. The output voltage of OP1 is proportional to the sum of these input signals. The output voltage of OP1 can be represented as $Vop1 = -(\frac{R2}{R1} \times Vop3 + \frac{R2}{R1} \times Vdrive)$, where Vop1/Vop3 is the output voltage of op1/op3 and Vdrive is the input driving voltage. After electrical actuation, piezoelectric current (I_p) will pass through the PMUT and be converted into output voltage through the current-to-voltage converter, which can be calculated as $Vout = -I_p \times Riv$. Then, the output voltage goes through the non-inverter amplifier and is amplified to the $Vop3 = \frac{R4+R3}{R3} \times Vout$. By combining the above equations, the transfer function of the quality factor increasing circuit will be:

$$H(s) = \frac{Vout(s)}{V_{drive}(s)} = \frac{-Riv}{Zm(s) - \frac{R2}{R1} \times \frac{R4+R3}{R3} \times Riv} \tag{5.1}$$

, where $Zm(s)$ is the impedance of the motional branch of the PMUT and it is equal to $Zm(s) = \frac{L_m C_m S^2 + R_m C_m S + 1}{C_m S}$. At the resonance frequency, the motional capacitor and inductor will cancel each other, and the impedance $Zm(s) = Rm$. By applying this circuit, the effective quality factor is derived as follows:

$$Q_{eff} = \frac{1}{R_m - \frac{R2}{R1} \times \frac{R4+R3}{R3} \times Riv} \sqrt{\frac{L_m}{C_m}} \tag{5.2}$$

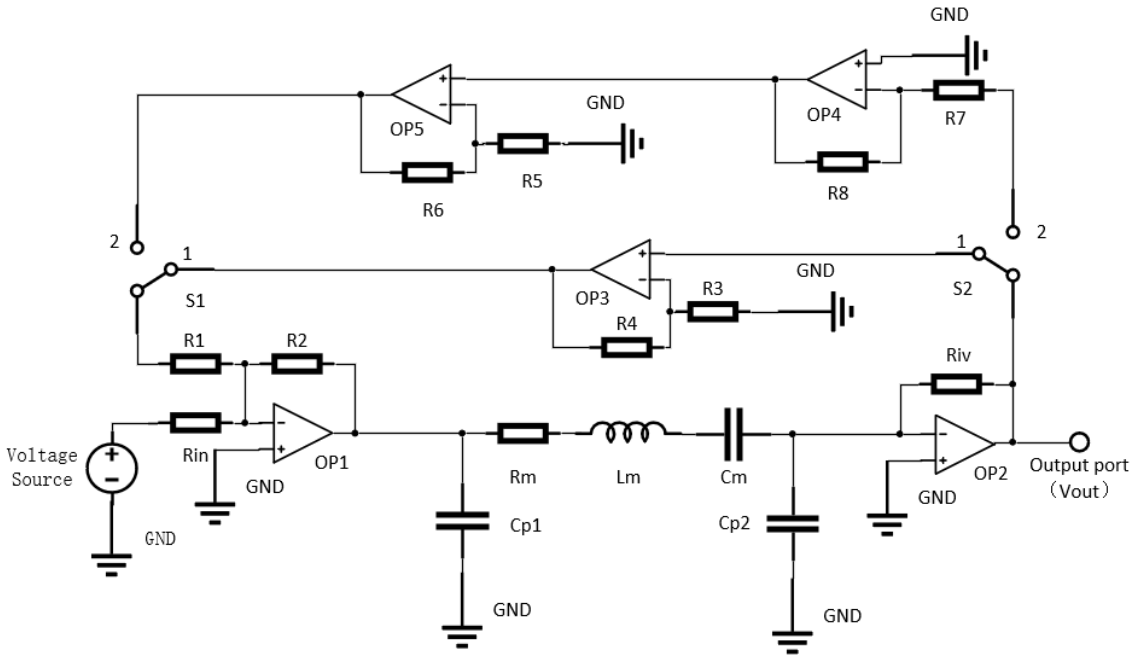

Figure 5.2: Increasing Q /Bandwidth circuit with driving voltage input

For the circuit simulation, LTspice was used. LTspice is a SPICE-based analog electronic circuit simulator commonly employed for simulating and analyzing the behavior of electronic circuits. Figure 5.3

is the circuit setup in simulation, there are a few differences compared with the schematic. C1, C2, and C3 are capacitors for creating a pole to increase stability of the opamps. Cc and Rc represent a capacitor and resistor, respectively, used for lag compensation at lower signal gain, as specified by the requirements in the LT1226 Operational Amplifier datasheet.

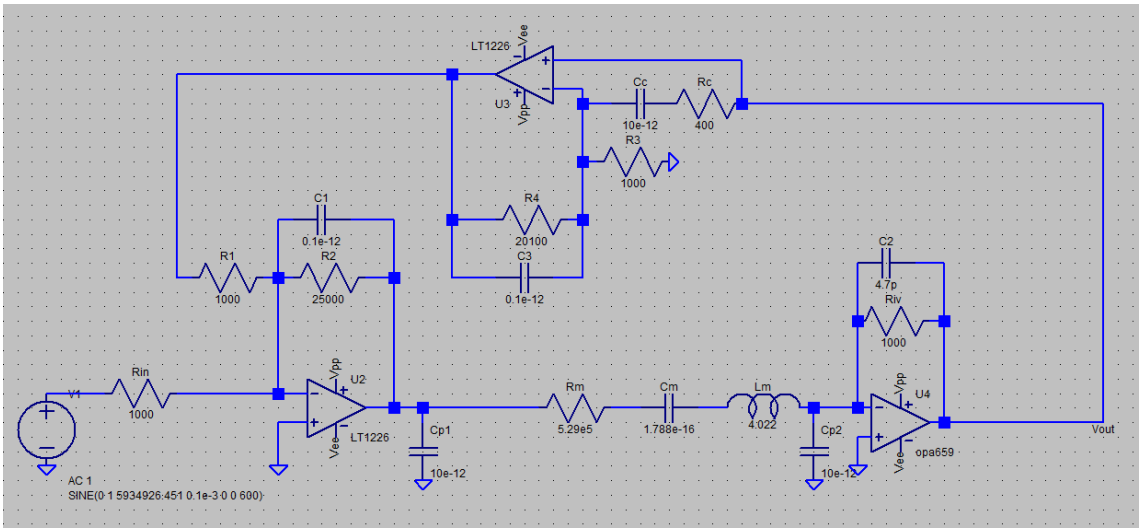

Figure 5.3: Quality factor increasing circuit in LTspice

Based on the circuit configuration, the driving voltage was set as a sinusoidal signal with a 1-volt amplitude, a resonance frequency of 5.934 MHz, a delay of 0.1 ms, and 600 cycles. The corresponding simulation results are presented in the figure 5.4. Vout1, Vout2, and Vout3 are different results from different resistor values and the Vopen is the circuit without feedback.

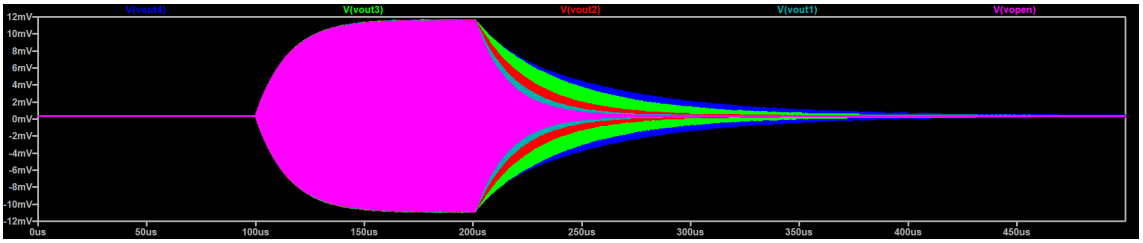

Figure 5.4: Quality factor increasing circuit simulation results in LTspice

In this simulation, four different resistor values were selected to demonstrate varying quality factors. The corresponding voltage output for each resistor can be found in Table 5.1. For the last row, 'Vopen' means the circuit is set to the open loop, and it will measure the original PMUT quality factor. According to the simulation, the decay time increases as the effective Rm decreases. The simulated quality factor (Q_{sim}) and the calculated quality factor(Q_{theory}) based on the equation 5.2 are also in the table 5.1. The discrepancy between the theoretical and simulated quality factors grows larger when the effective Rm becomes significantly lower than the original Rm.

	R2(ohm)	R4(ohm)	Riv(ohm)	Rm_{eff}	Q_{theory}	Q_{sim}
Vout4	25e3	20.1e3	1e3	1.5e3	10e4	986
Vout3	20e3	20e3	1e3	1.1e5	1376	747
Vout2	15e3	15e3	1e3	2.73e5	549	489
Vout1	10e3	10e3	1e3	4.19e5	357	367
Vopen	25e3	\	1e3	5.93e5	283	280

Table 5.1: Different resistor values setup with quality factor in theory and simulation with increasing quality factor circuit (The simulated quality factor (Q_{sim}) based on the simulation and the calculated quality factor(Q_{theory}) based on the equation 5.2)

5.2. Quality factor decreasing circuit

In the quality factor decreasing circuit, Switch 1 (S1) and Switch 2 (S2) are set to port 2. Compared to the quality factor enhancement configuration, this feedback loop includes an additional inverting amplifier, OP4, which alters the sign of the output voltage (Vout). The output of OP4 is given by $Vop4 = -(\frac{R8}{R7} \times Vout)$. Similarly, OP5 operates in the same manner as OP3, with its output voltage expressed as $Vop5 = \frac{R6+R5}{R5} \times Vop4$. By combining the above equations, the transfer function of the quality factor decreasing circuit is derived as follows:

$$H(s) = \frac{Vout(s)}{V_{drive}(s)} = \frac{-Riv}{Zm(s) + \frac{R2}{R1} \times \frac{R8}{R7} \frac{R6+R5}{R5} \times Riv} \tag{5.3}$$

Similar to the quality factor enhancement circuit, the effective quality factor at the resonance frequency can be expressed as:

$$Q_{eff} = \frac{1}{R_m + \frac{R2}{R1} \times \frac{R8}{R7} \frac{R6+R5}{R5} \times Riv} \sqrt{\frac{L_m}{C_m}} \tag{5.4}$$

The circuit setup is shown in 5.5. In this configuration, several modifications have been made, including the addition of capacitors C1, C2, C4, and C5 to introduce a pole for improving the stability of the opamps. For OP4, based on the LT1226 datasheet, the operational amplifier requires compensation at lower closed-loop gains. As a result, an extra resistor has been added to ensure that $R8 \geq 24 \times (R7||Rc)$.

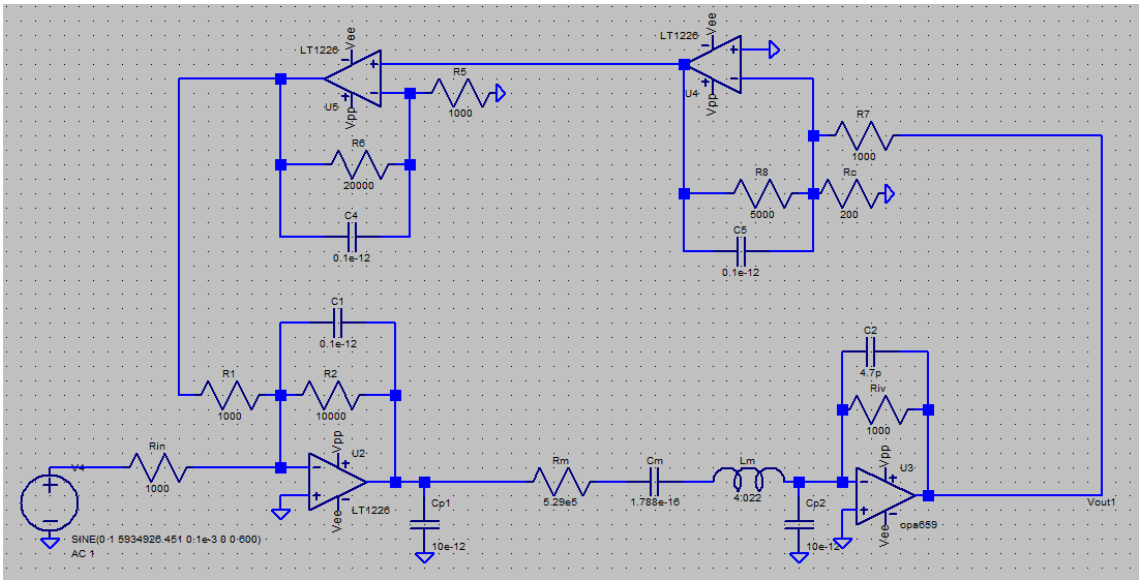

Figure 5.5: Quality factor decreasing circuit in LTspice

Based on the circuit configuration, the driving voltage was set as a sinusoidal signal with a 1-volt amplitude, a resonance frequency of 5.934 MHz, a delay of 0.1 ms, and 600 cycles. The driving voltage

setting is the same as the increasing quality factor circuit's driving voltage setting. The results are shown in figure 5.6.

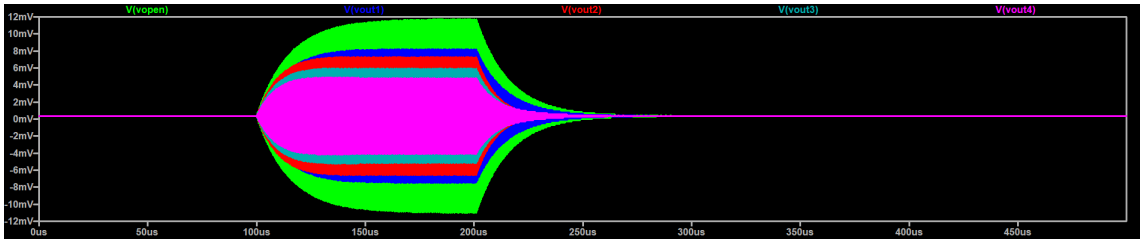

Figure 5.6: Quality factor decreasing circuit simulation results in LTspice

In this simulation, 4 different resistor values were chosen to show the various quality factors. The corresponding voltage output for each resistor can be found in Table 5.2. Based on the simulation, increasing the gain leads to a decrease in the quality factor (Q_{sim}), consistent with the theoretical quality factor (Q_{theory}) derived from equation 5.4. However, when the gain reaches certain values, the output voltage will become smaller than the noise value, which will influence the smallest quality factor that can be achieved.

	R2(ohm)	R6(ohm)	Riv(ohm)	R8(ohm)	Rm_{eff}	Q_{theory}	Q_{sim}
Vout4	10e3	25e3	1e3	5e3	1.829e6	82	145
Vout3	10e3	20e3	1e3	5e3	1.579e6	94	153
Vout2	10e3	15e3	1e3	5e3	1.329e6	112	181
Vout1	10e3	10e3	1e3	5e3	1.079e6	139	231
Vopen	10e3	\	1e3	\	5.29e5	283	280

Table 5.2: Different resistor values setup with quality factor in theory and simulation with decreasing circuit (The simulated quality factor (Q_{sim}) based on the simulation and the calculated quality factor(Q_{theory}) based on the equation 5.4)

6

Commercial PMUT with increasing/decreasing quality factor circuit test results

6.1. Increasing/Decreasing quality factor circuit with acoustic actuation

In Chapter 4, the electrical characteristics of the PMUT in the air were tested, and it was found that the electrical coupling between the PMUT and the ultrasound transducer used to excite it was too large. As a result, the signal generated by the PMUT due to acoustic vibrations was too weak to be observed. However, we still conducted tests using the circuit to verify our hypothesis. Like the PMUT acoustic test, the circuit setup requires a function generator, oscilloscope, ultrasound transducer, and a power supply. The test setup is shown in figure 6.1a, the circuit for testing is shown in figure 5.1, and the PCB of the circuit can be found in figure C.4 and C.5. After the acoustic actuation test by ultrasound transducer, we achieved similar results from PMUT in air acoustic test results in figure 6.1b. This indicates that acoustic actuation by the ultrasound transducer is unable to cause the PMUT to generate a current, rendering the acoustic actuation test unfeasible.

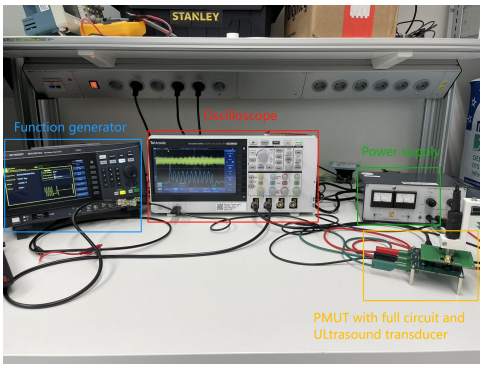

(a) PMUT with full circuit test setup

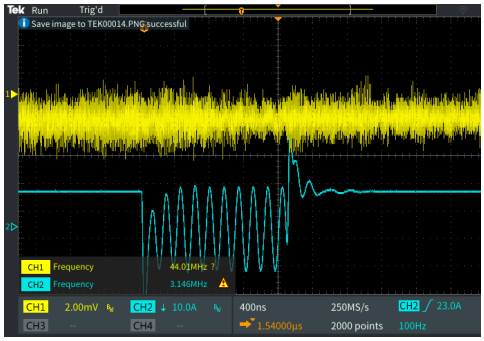

(b) Full circuit test result with acoustic actuation

Figure 6.1: PMUT acoustic actuation with full circuit test setup and test result (The blue curve represents the input voltage applied on the ultrasound transducer, while the yellow curve represents the generated output voltage after the increasing circuit from $PMUT_2$ in air acoustic actuation measurement)

6.2. Increasing/Decreasing quality factor circuit with electrical actuation

Due to the poor performance of PMUT in acoustically excited circuits, to verify the feasibility of using electronic feedback to alter the quality factor of the PMUT, the circuit will use driving voltage for excitation, and the control of the quality factor will be achieved by adjusting the resistance value of certain resistors in the circuit.

6.2.1. Increasing quality factor circuit with electrical actuation

Like the circuit setup in figure 5.2, when switch 1 (S1) and switch (S2) are connected with port 1, the circuit is set to the increasing quality factor mode. After the test, the quality factor from the test results is obtained by treating the system as a single-degree-of-freedom oscillator, allowing the measurement output voltage to be modeled by the equation below [26].

$$Vout(t) = A \times e^{\frac{-t}{\tau}} \times cos(W_d t + \phi_0) \tag{6.1}$$

, Where t represents time, A is initial amplitude, τ is decay time constant and $\tau = \frac{2Q}{2\pi f_n}$, $w_d = 2\pi f_n \sqrt{1 - \frac{1}{4Q^2}}$. After collecting the data, the test results will be fitted. During this process, the output voltage is normalized to facilitate easier observation of the decay time. Although the variation of decay time is small, we still achieve the desired function of using electronic feedback to increase the quality factor of PMUT.

Since the change in the quality factor during testing was not as significant as expected, open-loop (figure 6.2) and two sets of varying data (figure 6.3 and figure 6.4) will be selected for comparison after the fitting. In these figures, the blue line represents the fitted curve and the red line represents the original data. The results are in figure 6.5, resistor values with corresponding Quality factor in simulation and in theory are in the table 6.1.

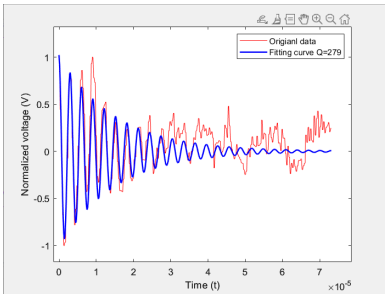

Figure 6.2: Open loop Q fitting result (The blue curve represents the fitted data, while the red curve represents the original data.)

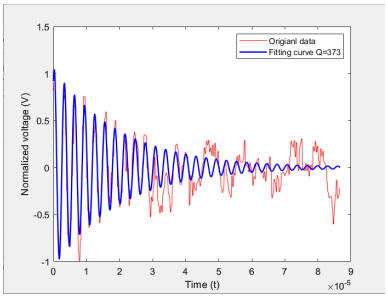

Figure 6.3: Set1 increasing Q fitting result (The blue curve represents the fitted data, while the red curve represents the original data.)

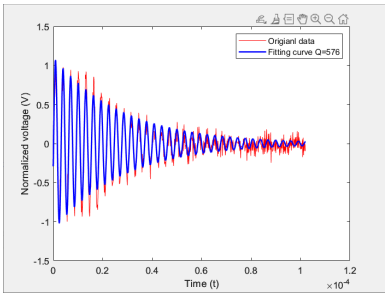

Figure 6.4: Set2 increasing Q fitting result (The blue curve represents the fitted data, while the red curve represents the original data.)

	R2 kohm	R4(kohm)	Rin(kohm)	Rm_{eff}(kohm)	Q_{meas}	Q_{sim}	Q_{theory}
SET2	25	20.1	1	1.5	576	886	10e4
SET1	20	20	1	110	373	747	1376
Vopen	10	\	1	529	279	280	283

Table 6.1: Different resistor values with quality factor in test (Q_{meas}), simulation (Q_{sim}), and theory (Q_{theory}) with Increasing quality factor circuit

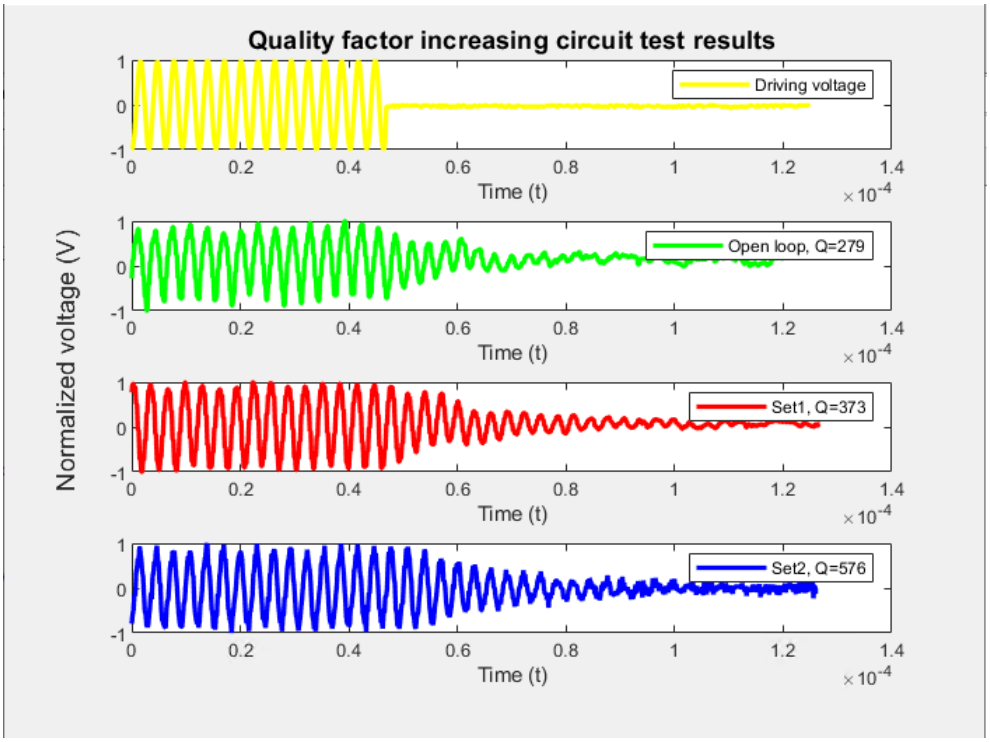

Figure 6.5: Increasing quality factor circuit with electrical actuation with different resistor values

6.2.2. Decreasing quality factor circuit with electrical actuation

Switch 1 (S1) and Switch 2 (S2) are connected to port 2 for the decreasing circuit. By using different resistor values, the circuit can achieve varying levels of reduced quality factor. Similar to the increasing circuit quality factor fitting method, the fitting curve of different resistors: set1 (figure 6.6) and set2 (figure 6.7). The test results and corresponding values are shown in figure 6.9 and table 6.2. As the gain increases further, the quality factor continues to decrease. However, when the output voltage approaches the noise level, changes in the quality factor become undetectable. For instance, in Figure 6.8, the blue curve obtained using resistor values from Set3, shows that the output voltage becomes indistinguishable.

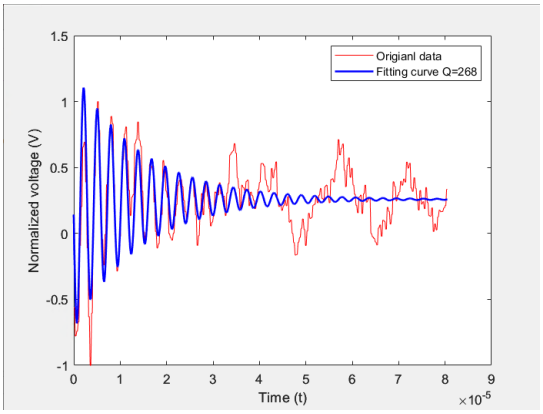

Figure 6.6: Set1 decreasing Q fitting result (The blue curve represents the fitted data, while the red curve represents the original data.)

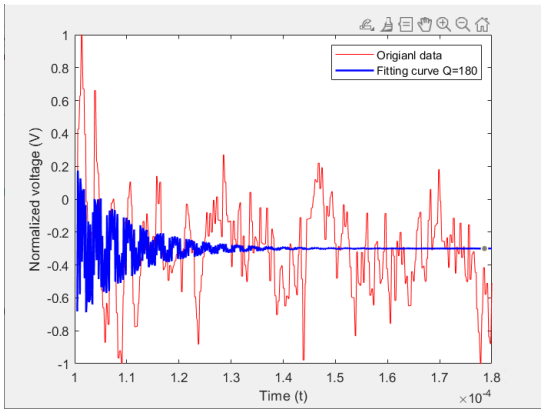

Figure 6.7: Set2 decreasing Q fitting result (The blue curve represents the fitted data, while the red curve represents the original data.)

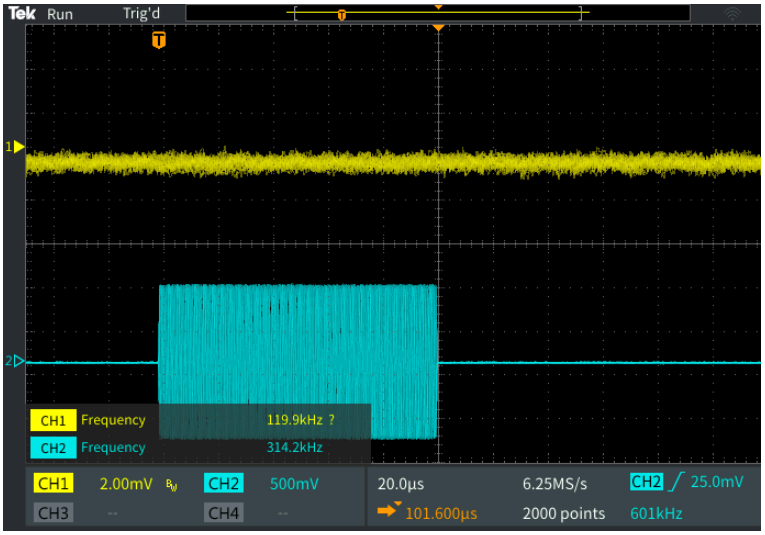

Figure 6.8: The decreasing quality factor circuit with resistor value Set3 shows undetectable quality factor (The blue curve represents the input voltage applied on the circuit, while the yellow curve represents the output voltage from the decreasing quality factor circuit)

	R2 kohm	R6(kohm)	Rin(kohm)	R8(Kohm)	Rm_{eff}(kohm)	Q_{meas}	Q_{sim}	Q_{theory}
SET 3	10	25	1	5	1829	\	145	82
SET 2	10	20	1	5	1579	180	153	94
SET 1	10	15	1	5	1329	269	181	112
Vopen	10	\	1	5	529	279	280	283

Table 6.2: Different resistor values with quality factor in test (Q_{meas}), simulation (Q_{sim}), and theory (Q_{theory}) with decreasing quality factor circuit

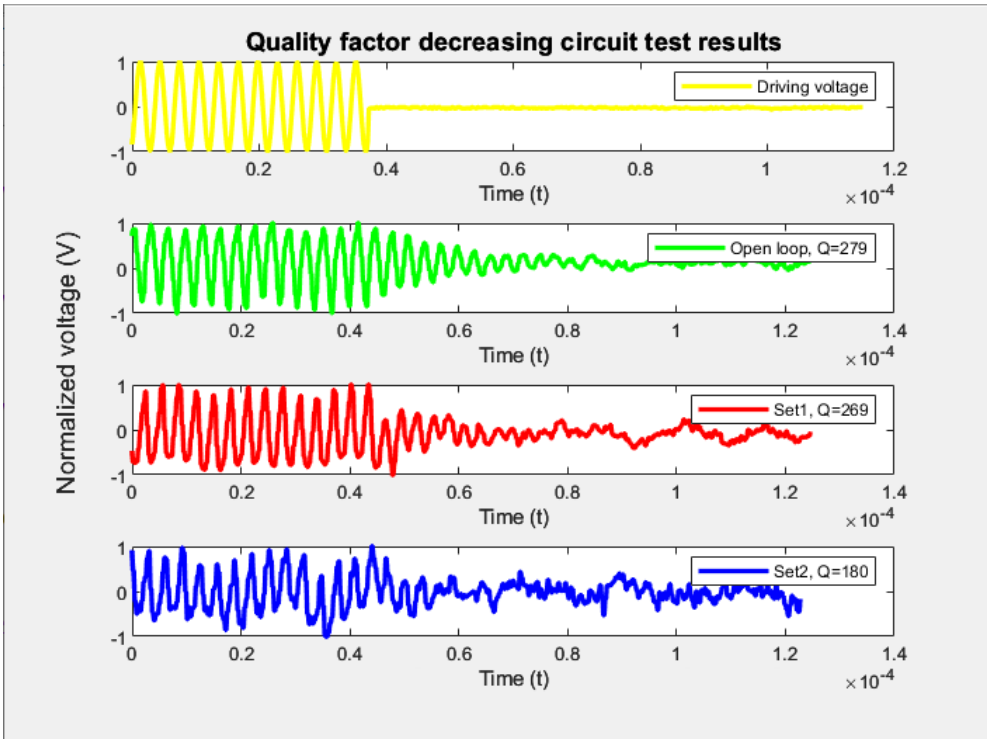

Figure 6.9: Decreasing Quality factor circuit with electrical actuation with different resistor values

7

Conclusion

In ultrasound transducer design, there is a constant trade-off between sensitivity and bandwidth. In ultrasound imaging, this translates to a conflict between image contrast and resolution. Since PMUTs have fixed parameters after fabrication, they are typically non-tunable for adaptation to different scenarios. The objective of this thesis was to use electronic feedback to adjust the quality factor of fabricated PMUTs. In this project, the writer utilized an ultrasound transducer for acoustic actuation of the PMUT to attempt to modify the quality factor. Additionally, a voltage source was applied to the circuit input for electrical actuation of the PMUT, aiming to tune the quality factor.

Before testing the PMUT in the circuit, the writer needed to verify the PMUT's functionality. A probe station was used to select working devices, and a VNA was employed to obtain the S12 data for fitting the motional branch of the PMUT. However, during measurement, the PMUT exhibited unusual behavior, where the anti-resonance frequency was lower than the resonance frequency in S12. By applying the multi-mode equivalent circuit model for fitting, the equivalent resistance, inductance, and capacitance were determined. These values will be used to select resistor values in the circuit to adjust the effective resistance and tune the quality factor.

In the acoustic actuation circuit measurement, the current produced by the piezoelectric effect from acoustic actuation is weaker than the unwanted signal, with one of the main sources of interference being electrical coupling. Due to the limited number of remaining PMUTs for wire bonding and insufficient time to reduce or eliminate the electrical coupling effect, electrical actuation was used as an alternative method to validate this concept.

In the electrical actuation circuit measurement, both the increasing and decreasing quality factor circuits demonstrated the potential of electronic feedback control for tuning the quality factor. However, the observed variation in the increasing quality factor circuit did not fully align with expectations. Discrepancies were observed between the measured quality factor results and the calculated values as the gain increased. One potential reason for this is that a phase shift in the feedback signal may have contributed to the reduction of the desired quality factor. In the decreasing quality factor circuit, the measured results were closely consistent with the calculated values as the gain increased.

In summary, the feasibility of this approach has been demonstrated through tests involving electrical actuation. However, there is still room for improvement in the increasing quality factor to ensure that the test results align consistently with the theoretical values of quality factor.

8

Discussion and future works

The primary focus of this work was on using electronic feedback to control the quality factor of the PMUT. While the main concept has been validated, there is still room for improvement regarding the undetectable results from the PMUT acoustic actuation tests and the undesired outcomes from the electrical actuation tests.

8.1. Improvement on PMUT acoustic actuation tests

- During the acoustic measurement, the ultrasound transducer was not characterized. Therefore, a more thorough acoustic evaluation of the ultrasound transducer should be carried out to ensure that the PMUT can effectively receive the desired acoustic signal.
- From the acoustic measurement, the electrical coupling exists between the ultrasound transducer as well as the PMUT's pads and PCB's traces. To mitigate such unwanted effects, it is advisable to shield both the ultrasound transducer and the PMUT with ground metal to block electrical coupling from the ultrasound transducer to the trace.
- An effective PCB design can help reduce electrical coupling. For instance, a 4-layer PCB is recommended, with traces positioned between ground layers instead of on the topmost layer, which could further minimize electrical coupling.

8.2. Improvement on PMUT electrical actuation tests

- From the electrical actuation circuit test, the increased quality factor was lower than anticipated. It may stem from the PMUT itself. During the analysis of the PMUT using a VNA to build an equivalent circuit model, an analysis of Y12 through the VNA revealed the presence of anti-resonance frequencies, which appeared before the resonance frequency. Generally, a PMUT 's resonance frequency is always higher than the anti-resonance frequency. This discrepancy suggests that the equivalent circuit model may not fully represent the PMUT, leading to differences between the expected equivalent resistance and the results obtained from fitting, ultimately affecting the control of resistance values in the feedback circuit.
- Beside the equivalent circuit model, one possible main reason is the feedback signal's phase shift. Based on the equation 3.2 and 3.3, the external feedback (F_{ext}) needs to maintain a 90-degree phase shift difference between the driving force (F_{drive}). When F_{ext} has a 90-degree phase shift, it can be represented as $F_{ext}(s) = b_{feed}s$. However, for a more general phase relationship θ between the external feedback and the driving force, it can be expressed as [53]:

  $$F_{ext} \propto G \times |sin(\theta)|$$

  where G is the gain of the op-amp. From this relationship, it's clear that when the phase shift deviates from exactly 90 degrees, the gain of the feedback is reduced, which lowers the value of b_{feed} and consequently results in a smaller quality factor. Therefore, incorporating a phase

shifter to adjust the phase shift and a phase-locked loop to maintain a 90° phase difference can significantly enhance the performance of the quality factor tuning circuit [53]. To demonstrate the concept of using a phase shift circuit to increase the quality factor, an ideal phase shift was implemented in the circuit, as shown in Figure 5.3. The phase shifter used resistors Rs = Rs2 = 1000 ohms, R7 = 50 ohms, and capacitor C7 = 1nF. The feedback resistors (R2 = 25K ohms, R4 = 20.1K ohms, Riv = 1K ohm) were set to the same values as Vout4 in Table 5.1. The final simulated circuit can be found in figure 8.1. The voltage V(Vout shift) represents the test results of the increasing quality factor circuit with an added phase shifter, while V(Vout) shows the test results of the same circuit without the phase shifter. These results are illustrated in Figure 8.2 and the quality factor of V(Vout shift) is 1.48e4 which is closer to the quality factor(10e4) in theory compared to the V(Vout) without using the phase shifter.

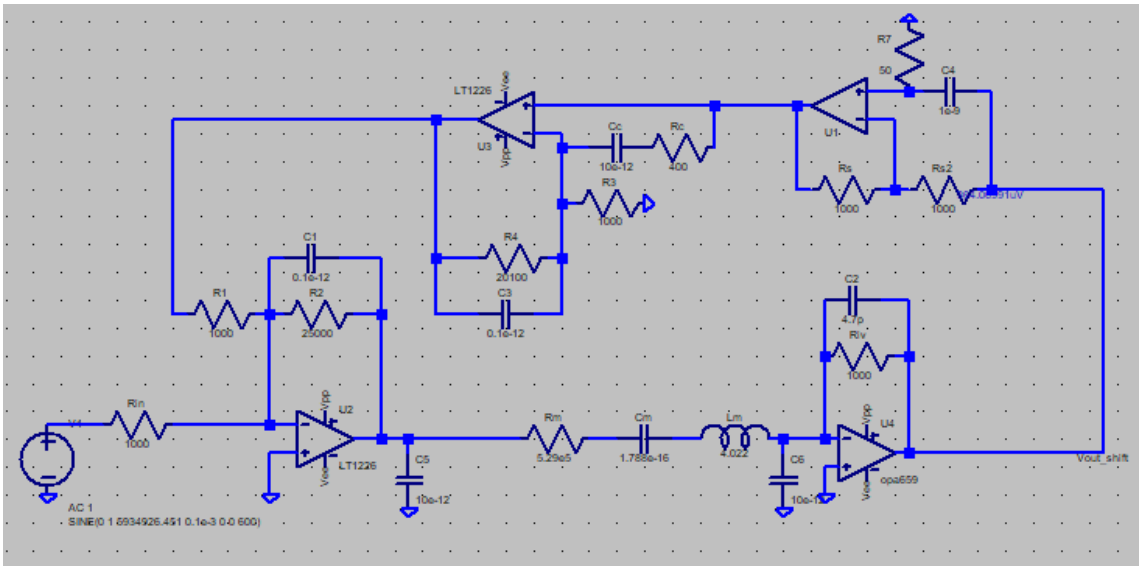

Figure 8.1: Quality factor increasing circuit with ideal additional phase shifter in LTspice

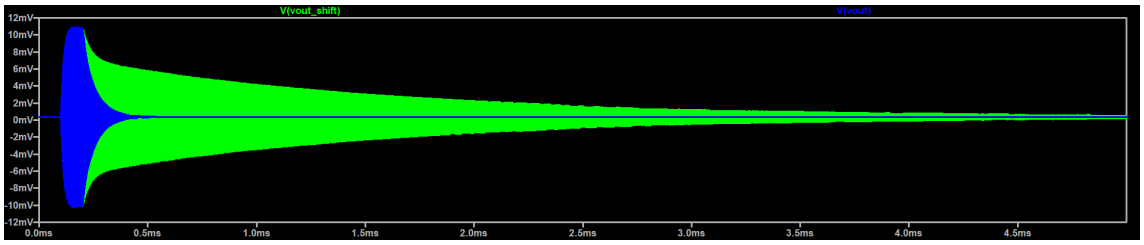

Figure 8.2: Quality factor increasing circuit with additional phase shifter in LTspice test results The green voltage curve, V(Vout shift), represents the test results of the increasing quality factor circuit with the phase shifter added, while the blue curve, V(Vout), shows the results of the same circuit without the phase shifter.

References

[1] R. Abdolvand et al. “Micromachined resonators: a review”. In: Micromachines 7 (9 2016), p. 160. DOI: 10.3390/mi7090160.

[2] H. L. Abrams. “Health risks from exposure to low levels of ionizing radiation”. In: (2006). DOI: 10.17226/11340.

[3] F. Akasheh et al. “Development of piezoelectric micromachined ultrasonic transducers”. In: Sensors and Actuators A: Physical 111 (2-3 2004), pp. 275–287. DOI: 10.1016/j.sna.2003.11.022.

[4] Antonio Arnau and David Soares. “Fundamentals of piezoelectricity”. In: Piezoelectric transducers and applications. Springer, 2009, pp. 1–38.

[5] M. Berger, Q. Yang, and A. Maier. “X-ray imaging”. In: Lecture Notes in Computer Science (2018), pp. 119–145. DOI: 10.1007/978-3-319-96520-8_7.

[6] Harmeet Bhugra and Gianluca Piazza. “Design of Piezoelectric MEMS Resonators”. In: Piezoelectric MEMS resonators. Springer International Publishing, 2017.

[7] Harmeet Bhugra and Gianluca Piazza. “Flexural Piezoelectric Resonators”. In: Piezoelectric MEMS resonators. Springer International Publishing, 2017.

[8] Y. Birjis et al. “Piezoelectric micromachined ultrasonic transducers (pmuts): performance metrics, advancements, and applications”. In: Sensors 22 (23 2022), p. 9151. DOI: 10.3390/s22239151.

[9] C. Cheng et al. “Thin film pzt-based pmut arrays for deterministic particle manipulation”. In: IEEE Transactions on Ultrasonics, Ferroelectrics, and Frequency Control 66 (10 2019), pp. 1606–1615. DOI: 10.1109/tuffc.2019.2926211.

[10] “Clinical ultrasound”. In: (2011). DOI: 10.1016/c2010-1-66391-2.

[11] Ajay Dangi and Rudra Pratap. “System level modeling and design maps of PMUTs with residual stresses”. In: Sensors and Actuators A: Physical 262 (2017), pp. 18–28. ISSN: 0924-4247. DOI: https://doi.org/10.1016/j.sna.2017.05.006. URL: https://www.sciencedirect.com/science/article/pii/S0924424716308391.

[12] M.-A. Dubois and P. Muralt. “PZT thin film actuated elastic fin micromotor”. In: IEEE Transactions on Ultrasonics, Ferroelectrics, and Frequency Control 45.5 (1998), pp. 1169–1177. DOI: 10.1109/58.726440.

[13] Benjamin E. Eovino, Sina Akhbari, and Liwei Lin. “Broadband ring-shaped PMUTS based on an acoustically induced resonance”. In: 2017 IEEE 30th International Conference on Micro Electro Mechanical Systems (MEMS). 2017, pp. 1184–1187. DOI: 10.1109/MEMSYS.2017.7863627.

[14] V. Ferrari, D. Marioli, and A. Taroni. “Improving the accuracy and operating range of quartz microbalance sensors by a purposely designed oscillator circuit”. In: Proceedings of the 17th IEEE Instrumentation and Measurement Technology Conference [Cat. No. 00CH37066] (). DOI: 10.1109/imtc.2000.848670.

[15] P J French and P M Sarro. “Surface versus bulk micromachining: the contest for suitable applications”. In: Journal of Micromechanics and Microengineering 8.2 (June 1998), p. 45. DOI: 10.1088/0960-1317/8/2/002. URL: https://dx.doi.org/10.1088/0960-1317/8/2/002.

[16] A. Guedes et al. “Aluminum nitride pMUT based on a flexurally-suspended membrane”. In: 2011 16th International Solid-State Sensors, Actuators and Microsystems Conference. 2011, pp. 2062–2065. DOI: 10.1109/TRANSDUCERS.2011.5969223.

[17] A. Hajati et al. “Three-dimensional micro electromechanical system piezoelectric ultrasound transducer”. In: Applied Physics Letters 101 (25 2012). DOI: 10.1063/1.4772469.

[18] C. J. Harvey et al. “Advances in ultrasound”. In: Clinical Radiology 57 (3 2002), pp. 157–177. DOI: 10.1053/crad.2001.0918.

[19] S. Hughes. “Medical ultrasound imaging”. In: Physics Education 36 (6 2001), pp. 468–475. DOI: 10.1088/0031-9120/36/6/304.

[20] Jose Joseph, Bo Ma, and B. T. Khuri-Yakub. “Applications of Capacitive Micromachined Ultrasonic Transducers: A Comprehensive Review”. In: IEEE Transactions on Ultrasonics, Ferroelectrics, and Frequency Control 69.2 (2022), pp. 456–467. DOI: 10.1109/TUFFC.2021.3112917.

[21] J. Jung et al. “Review of piezoelectric micromachined ultrasonic transducers and their applications”. In: Journal of Micromechanics and Microengineering 27 (11 2017), p. 113001. DOI: 10.1088/1361-6439/aa851b.

[22] Cyril Baby Karuthedath et al. “Design and Fabrication of Aluminum Nitride Piezoelectric Micromachined Ultrasonic Transducers for Air Flow Measurements”. In: 2019 IEEE International Ultrasonics Symposium (IUS). 2019, pp. 2489–2492. DOI: 10.1109/ULTSYM.2019.8925544.

[23] Butrus T Khuri-Yakub and Ömer Oralkan. “Capacitive micromachined ultrasonic transducers for medical imaging and therapy”. In: Journal of Micromechanics and Microengineering 21.5 (Apr. 2011), p. 054004. DOI: 10.1088/0960-1317/21/5/054004. URL: https://dx.doi.org/10.1088/0960-1317/21/5/054004.

[24] Butrus T. Khuri-yakub, Omer Oralkan, and Mario Kupnik. “Next-gen ultrasound”. In: IEEE Spectrum 46.5 (2009), pp. 44–54. DOI: 10.1109/MSPEC.2009.4907385.

[25] M. Kucera et al. “Lock-in driven quality factor enhancement with parasitic effect compensation of a self-actuated piezoelectric MEMS cantilever”. In: 2012 IEEE International Ultrasonics Symposium. 2012, pp. 2195–2198. DOI: 10.1109/ULTSYM.2012.0548.

[26] M. Kučera et al. “q-factor enhancement for self-actuated self-sensing piezoelectric mems resonators applying a lock-in driven feedback loop”. In: Journal of Micromechanics and Microengineering 23 (8 2013), p. 085009. DOI: 10.1088/0960-1317/23/8/085009.

[27] Yuri Kusano et al. “Effects of DC Bias Tuning on Air-Coupled PZT Piezoelectric Micromachined Ultrasonic Transducers”. In: Journal of Microelectromechanical Systems 27.2 (2018), pp. 296–304. DOI: 10.1109/JMEMS.2018.2797684.

[28] K.M. Lakin. “Modeling of thin film resonators and filters”. In: 1992 IEEE MTT-S Microwave Symposium Digest. 1992, 149–152 vol.1. DOI: 10.1109/MWSYM.1992.187931.

[29] W. Lee and Y. Roh. “Ultrasonic transducers for medical diagnostic imaging”. In: Biomedical Engineering Letters 7 (2 2017), pp. 91–97. DOI: 10.1007/s13534-017-0021-8.

[30] Y. Lemoigne, A. Caner, and G. Rahal. “Physics for medical imaging applications”. In: NATO Science Series (2007). DOI: 10.1007/978-1-4020-5653-6.

[31] J. Li et al. “Design and fabrication of piezoelectric micromachined ultrasound transducer (pmut) with partially-etched zno film”. In: Sensors 17 (6 2017), p. 1381. DOI: 10.3390/s17061381.

[32] J. Li et al. “Recent advancements in ultrasound transducer: from material strategies to biomedical applications”. In: BME Frontiers 2022 (2022). DOI: 10.34133/2022/9764501.

[33] Xinxin Liu et al. “A High-Performance Square pMUT for Range-finder”. In: 2018 IEEE 13th Annual International Conference on Nano/Micro Engineered and Molecular Systems (NEMS). 2018, pp. 106–109. DOI: 10.1109/NEMS.2018.8556913.

[34] Yipeng Lu et al. “Broadband piezoelectric micromachined ultrasonic transducers based on dual resonance modes”. In: 2015 28th IEEE International Conference on Micro Electro Mechanical Systems (MEMS). 2015, pp. 146–149. DOI: 10.1109/MEMSYS.2015.7050907.

[35] Yipeng Lu et al. “High frequency piezoelectric micromachined ultrasonic transducer array for intravascular ultrasound imaging”. In: 2014 IEEE 27th International Conference on Micro Electro Mechanical Systems (MEMS). 2014, pp. 745–748. DOI: 10.1109/MEMSYS.2014.6765748.

[36] J. W. Miller et al. “Effective quality factor tuning mechanisms in micromechanical resonators”. In: Applied Physics Reviews 5 (4 2018). DOI: 10.1063/1.5027850.

[37] V. M. d. Nascimento et al. “Influence of backing and matching layers in ultrasound transducer performance”. In: SPIE Proceedings (2003). DOI: 10.1117/12.479924.

[38] Nguyen and Howe. “Quality factor control for micromechanical resonators”. In: 1992 International Technical Digest on Electron Devices Meeting. 1992, pp. 505–508. DOI: 10.1109/IEDM.1992.307411.

[39] William D. O’Brien. “Ultrasound–biophysics mechanisms”. In: Progress in Biophysics and Molecular Biology 93.1 (2007). Effects of ultrasound and infrasound relevant to human health, pp. 212–255. ISSN: 0079-6107. DOI: https://doi.org/10.1016/j.pbiomolbio.2006.07.010. URL: https://www.sciencedirect.com/science/article/pii/S0079610706000915.

[40] C.G. Oakley and M.J. Zipparo. “Single crystal piezoelectrics: a revolutionary development for transducers”. In: 2000 IEEE Ultrasonics Symposium. Proceedings. An International Symposium (Cat. No.00CH37121). Vol. 2. 2000, 1157–1167 vol.2. DOI: 10.1109/ULTSYM.2000.921530.

[41] Andreas S. Panayides et al. “AI in Medical Imaging Informatics: Current Challenges and Future Directions”. In: IEEE Journal of Biomedical and Health Informatics 24.7 (2020), pp. 1837–1857. DOI: 10.1109/JBHI.2020.2991043.

[42] Y. Poplavko and Y. Yakymenko. “Piezoelectricity”. In: Functional Dielectrics for Electronics (2020), pp. 161–216. DOI: 10.1016/b978-0-12-818835-4.00005-5.

[43] Richard J. Przybyla et al. “In-Air Rangefinding With an AlN Piezoelectric Micromachined Ultrasound Transducer”. In: IEEE Sensors Journal 11.11 (2011), pp. 2690–2697. DOI: 10.1109/JSEN.2011.2157490.

[44] Yongqiang Qiu et al. “Piezoelectric Micromachined Ultrasound Transducer (PMUT) Arrays for Integrated Sensing, Actuation and Imaging”. In: Sensors 15.4 (2015), pp. 8020–8041. ISSN: 1424-8220. DOI: 10.3390/s150408020. URL: https://www.mdpi.com/1424-8220/15/4/8020.

[45] K. Roy, J. Lee, and C. Lee. “Thin-film pmuts: a review of over 40 years of research”. In: Microsystems Amp; Nanoengineering 9 (1 2023). DOI: 10.1038/s41378-023-00555-7.

[46] P.J. French S. Middelhoek S.A. Audet and G Vdovin. “3.2 Piezoelectricity”. In: Silicon Sensors. Delft University of Technology, 2022, pp. 137–141.

[47] S. Schmid, G. Villanueva, and M. L. Roukes. “Fundamentals of nanomechanical resonators”. In: (2016). DOI: 10.1007/978-3-319-28691-4.

[48] Jaibir Sharma et al. “Piezoelectric over Silicon-on-Nothing (pSON) process”. In: 2021 IEEE International Ultrasonics Symposium (IUS). 2021, pp. 1–4. DOI: 10.1109/IUS52206.2021.9593772.

[49] Ronald H Silverman, Emma Vinarsky, and D JACKSON COLEMAN. “The Effect of Transducer Bandwidth on Ultrasonic”. In: Retina 15 (1995), pp. 37–42.

[50] Katherine Smyth et al. “Analytic solution for N-electrode actuated piezoelectric disk with application to piezoelectric micromachined ultrasonic transducers”. In: IEEE Transactions on Ultrasonics, Ferroelectrics, and Frequency Control 60.8 (2013), pp. 1756–1767. DOI: 10.1109/TUFFC.2013.2756.

[51] J Soderkvist. “Similarities between piezoelectric, thermal and other internal means of exciting vibrations”. In: Journal of Micromechanics and Microengineering 3.1 (Mar. 1993), p. 24. DOI: 10.1088/0960-1317/3/1/006. URL: https://dx.doi.org/10.1088/0960-1317/3/1/006.

[52] T. L. Szabo. “Overview”. In: Diagnostic Ultrasound Imaging: Inside Out (2014), pp. 39–54. DOI: 10.1016/b978-0-12-396487-8.00002-1.

[53] J. Tamayo et al. “High-q dynamic force microscopy in liquid and its application to living cells”. In: Biophysical Journal 81 (1 2001), pp. 526–537. DOI: 10.1016/s0006-3495(01)75719-0.

[54] H. Tang et al. “Pulse-echo ultrasonic fingerprint sensor on a chip”. In: 2015 Transducers - 2015 18th International Conference on Solid-State Sensors, Actuators and Microsystems (TRANSDUCERS). 2015, pp. 674–677. DOI: 10.1109/TRANSDUCERS.2015.7181013.

[55] H. Tang et al. “Pulse-echo ultrasonic fingerprint sensor on a chip”. In: 2015 Transducers - 2015 18th International Conference on Solid-State Sensors, Actuators and Microsystems (TRANSDUCERS). 2015, pp. 674–677. DOI: 10.1109/TRANSDUCERS.2015.7181013.

[56] “Thoracic ultrasound and integrated imaging”. In: (2020). DOI: 10.1007/978-3-319-93055-8.

[57] S. Trolier-McKinstry and P. Muralt. “Thin film piezoelectrics for mems”. In: Journal of Electroceramics 12 (1/2 2004), pp. 7–17. DOI: 10.1023/b:jecr.0000033998.72845.51.

[58] Q. Wang et al. “Low thermal budget surface micromachining process for piezoelectric micromachined ultrasonic transducer arrays with in-situ vacuum sealed cavities”. In: 2018 Solid-State, Actuators, and Microsystems Workshop Technical Digest (2018), pp. 245–248. DOI: 10.31438/trf.hh2018.71.

[59] Qi Wang et al. “Design, Fabrication, and Characterization of Scandium Aluminum Nitride-Based Piezoelectric Micromachined Ultrasonic Transducers”. In: Journal of Microelectromechanical Systems 26.5 (2017), pp. 1132–1139. DOI: 10.1109/JMEMS.2017.2712101.

[60] Tao Wang, Takeshi Kobayashi, and Chengkuo Lee. “Broadband piezoelectric micromachined ultrasonic transducer (pMUT) using mode-merged design”. In: 10th IEEE International Conference on Nano/Micro Engineered and Molecular Systems. 2015, pp. 238–242. DOI: 10.1109/NEMS.2015.7147418.

[61] X. Wang et al. “Development of broadband high-frequency piezoelectric micromachined ultrasonic transducer array”. In: Sensors 21 (5 2021), p. 1823. DOI: 10.3390/s21051823.

[62] X. Wang et al. “Development of broadband high-frequency piezoelectric micromachined ultrasonic transducer array”. In: Sensors 21 (5 2021), p. 1823. DOI: 10.3390/s21051823.

[63] J. J. Wild. “Use of high-frequency ultrasonic waves for detecting changes of texture in living tissues”. In: The Lancet 257 (6656 1951), pp. 655–657. DOI: 10.1016/s0140-6736(51)92403-8.

[64] Zhipeng Wu et al. “Tuning Characteristics of AlN-Based Piezoelectric Micromachined Ultrasonic Transducers Using DC Bias Voltage”. In: IEEE Transactions on Electron Devices 69.2 (2022), pp. 729–735. DOI: 10.1109/TED.2021.3137766.

A

Code for fitting to obtain the equivalent circuit model

The data fitting code consists of three parts: the first part imports the data, the second part handles data fitting, and the third part defines the fitting function.

Below is the code for importing data.

```
clc;
clear;
% Input data
num=readmatrix('VNA-6MHZ2.csv','Range','A08:I1008');
f=num(:,1)';
s11=num(:,2)';
Phase_s11= num(:,3)';
s12= num(:,4)';
Phase_s12= num(:,5)';
s21= num(:,6)';
Phase_s21= num(:,7)';
s22= num(:,8)';
Phase_s22= num(:,9)';

%convert data to complex value
c_S11 = [10.^(s11/20) .* exp(1j*deg2rad(Phase_s11))];
c_S12 = [10.^(s12/20) .* exp(1j*deg2rad(Phase_s12))];
c_S21 = [10.^(s21/20) .* exp(1j*deg2rad(Phase_s21))];
c_S22 = [10.^(s22/20) .* exp(1j*deg2rad(Phase_s22))];

%convert data from s parameter to Y-parameter
z0 = 50;
s_params(1,1,:) = c_S11;
s_params(1,2,:) = c_S12;
s_params(2,1,:) = c_S21;
s_params(2,2,:) = c_S22;
y_params = s2y(s_params,z0);

% Y11
a = length(f);
Y11 = zeros(1,a);
Ymag11 = zeros(1,a);
Yph11 = zeros(1,a);
for i = 1:length(f)
    index = y_params(:,:,i);
    Y11(1,i) = index(1,1);
    Ymag11(1,i) = mag2db(abs(Y11(1,i)));
    Yph11(1,i) = phase(Y11(1,i))*180/pi;
end

% Y22
```

```
a = length(f);
Y22 = zeros(1,a);
Ymag22 = zeros(1,a);
Yph22 = zeros(1,a);
for i = 1:length(f)
    index = y_params(:,:,i);
    Y22(1,i) = index(2,2);
    Ymag22(1,i) = mag2db(abs(Y22(1,i)));
    Yph22(1,i) = phase(Y22(1,i))*180/pi;
end

% % Y12
a = length(f);
Y12 = zeros(1,a);
Ymag12 = zeros(1,a);
Yph12 = zeros(1,a);
for i = 1:length(f)
    index = y_params(:,:,i);
    Y12(1,i) = index(1,2);
    Ymag12(1,i) = mag2db(abs(Y12(1,i)));
%  Ymag12(1,i) = (abs(Y12(1,i)));
    Yph12(1,i) = phase(Y12(1,i))*180/pi;
end

% data fitting
  Y = [f;Ymag12;Yph12];
 [xx]=RLCequivNEW7(Y,1000);
```

Below is the code for fitting the data.

```

function [xx]=RLCequivNEW7(Y,n)
%[xx]=RLCequivNEW7(Y,n)
%
%Y is the data matrix with these rows:
%   Frequency in MHz.
%   Magnitude of Y21 in dB.
%   Phase of Y21 in degrees.
%n is the maximum number of iterations allowed.

Ymag=Y(2,:);
Yph=Y(3,:);

f=Y(1,:);
Y11=10.^(Ymag/20).*exp(1j*Yph*pi/180);

%Preliminary estimation of Q and fr
[m1,imax]=max(imag(Y11)./f);
[m2,imin]=min(imag(Y11)./f);
 fn=f(imax)%fn=1.06e9
fp=f(imin)%fp=1.12e9
fr=sqrt((fp^2+fn^2)/2);%fr=1.05e9
Q=2*fr^2/(fp^2-fn^2);%Q=100

%Preliminary estimation of input network parameters
% R01=1/real(Y11(1));
% C01=imag(Y11(1))/(2*pi*f(1));
% R1=1/(max(real(Y11))-1/R01);
% C1=1/(Q*R1*2*pi*fr);
% L1=Q*R1/(2*pi*fr);
%Rs=Rs_initial;
%Ls=Ls_initial;
 fs=5.92e6;
 C0=5e-16;
R1=3.8e3;
C1=7.6989e-17;
L1= 9.411;
Rp=1e8;
Rsp=31;
Ls=1e-8;
%  Cp calculated from Z parameter
```

```
Cp=9.5e-12;

L2=L1;
C2=C1*1e4;
R2=R1*100;



%Vector of parameters
x0=[R1 L1 L2 C2 R2];


%Fitting
options=optimset(...
                 'TolFun',0,'TolX',0,...
                 'MaxFunEvals',200000,'MaxIter',n,...
                 'Display','iter');
[xx,RESNORM,RESIDUAL,EXITFLAG,OUTPUT]=lsqcurvefit(@ComplexZequiv7,x0,f,[Ymag; Yph],[4.8e5
    ,0,0,0,0],[5.1e5,inf,inf,1,inf],options);

Ym=ComplexZequiv7(xx,f);

 Ymagm=mag2db(Ym(1,:));
  Yphm=Ym(2,:);

C1=1/((2*pi*fs)^2*xx(2))


%Plot the results
figure(1)
subplot(1,2,1);
plot(f,Ymag,'r-',f,Ymagm,'b-','LineWidth',2),grid
xlabel('Frequency␣(Hz)','FontSize',12);
ylabel('|Y12|(db)','FontSize',12)
subplot(1,2,2);
plot(f,Yph,'r-',f,Yphm,'b-','LineWidth',2),grid
xlabel('Frequency␣(Hz)','FontSize',12)
ylabel('phase(Y12)␣(deg)','FontSize',12)
hold on

Fitting_data = ["Rm";"Lm";"Cm";"Lm_s";"Cm_s";"Rm_s";];
Fitting_data = ["Rm";"Lm";"Cm";"Rm_s";"Lm_s";"Cm_s";];
results =[xx(1);xx(2);C1;xx(5);xx(3);xx(4)];
% unit=[ohm;H;F,ohm,H,F]
unit= ["ohm";"H";"F";"ohm";"H";"F"];
Fitting_results= table(Fitting_data,results,unit)




end
```

Below is the code for defining the equivalent circuit model.

```
function Y=ComplexZequiv7(x,f)
fs=5.923e6;
w=2*pi*f;
R1=x(1);
L1=x(2);
C1=1/((2*pi*fs)^2*L1);
L2=x(3);
C2=x(4);
R2=x(5);



%Y11
Y1=1./( R1+(1i.*w*L1)-1i./(w*C1) );
Y2=1./(R2+(1i.*w*L2)-1i./(w*C2));
Y11 = Y1 + Y2;
```

```
18
19 Y=[(abs(Y11)); (rad2deg((phase(Y11))))];
20
21 end
```

B

Code for fitting to obtain quality factor

The data fitting code consists of 2 parts: the first part imports the data and handles data fitting, and the second part defines the fitting function. Below is the code for importing data and fitting.

```
1
2  clc;
3  clear;
4  num=readmatrix('set2.CSV','Range','A300:I1507');
5  t1=num(:,1);
6  v1=num(:,2);
7
8  T=length(t1);
9  n=(max(t1)-min(t1))./(T-1);
10 t= zeros(T,1);
11 k=0;
12 for i=1:T
13     t(i,1)=k;
14     k=k+n;
15 end
16
17 N1 = ((v1-min(v1))/(max(v1)-min(v1))-0.5)*2;
18 %inital guess
19 Q=283;
20
21 Wn=5.934e6*2*pi;
22
23 A=2700;
24  W0=0;
25 d=0;
26
27
28
29 % fit
30 opt=optimoptions('lsqcurvefit');                % create default object for given fitter
31 opt=optimoptions(opt,'StepTolerance',1e-14,'MaxFunEvals',20000,'MaxIter',10000,'Display','
       iter');    % set the step tolerance to something other than default
32 options=optimset(...
33                  'TolFun',0,'TolX',0,...
34                  'MaxFunEvals',200000,'MaxIter',500,...
35                  'Display','iter');
36 x0=[Q Wn A W0 d];
37
38
39 [x,RESNORM,RESIDUAL,EXITFLAG,OUTPUT] = lsqcurvefit(@CompleZequiv,x0,t,N1,[0,0,0,-inf,-inf
       ],[],options);
40
41
42
43 Vfit= CompleZequiv(x,t);
44
```

```
figure(1)
plot(t,N1,'b')
 hold on
plot(t,Vfit, 'r', 'LineWidth',1.5)

Q=x(1)
```

Below is the code for the fitting function.

```

function V=ComplexZequiv(x,t)

Q=x(1);

Wn=x(2);

A=x(3);
 W0=x(4);
 Wd=Wn*sqrt(1-1./(4.*Q^2));
 d=x(5);

V= A.*exp(-t./(2.*Q./Wn)).*cos(Wd.*t+W0)+d;

end
```

C

PCB schematics and figures

PCB schematics and figures of the daughterboard and motherboard can be found in the below.

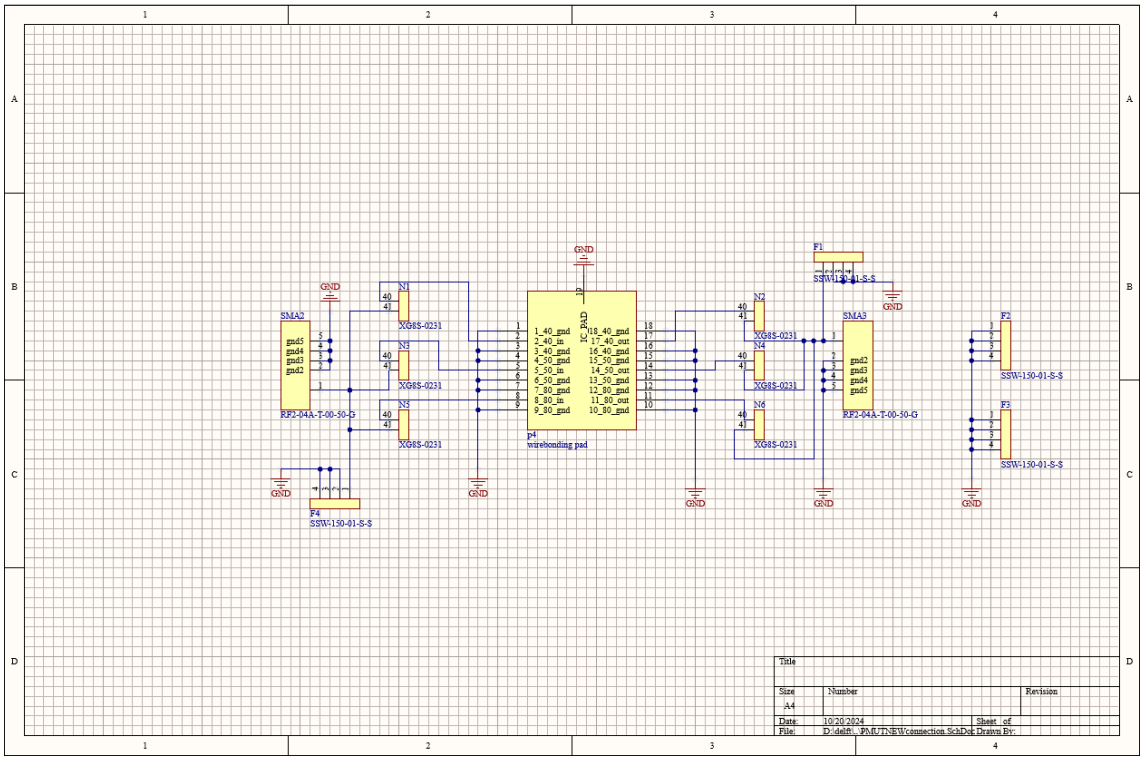

Figure C.1: PCB: daughter board schematic

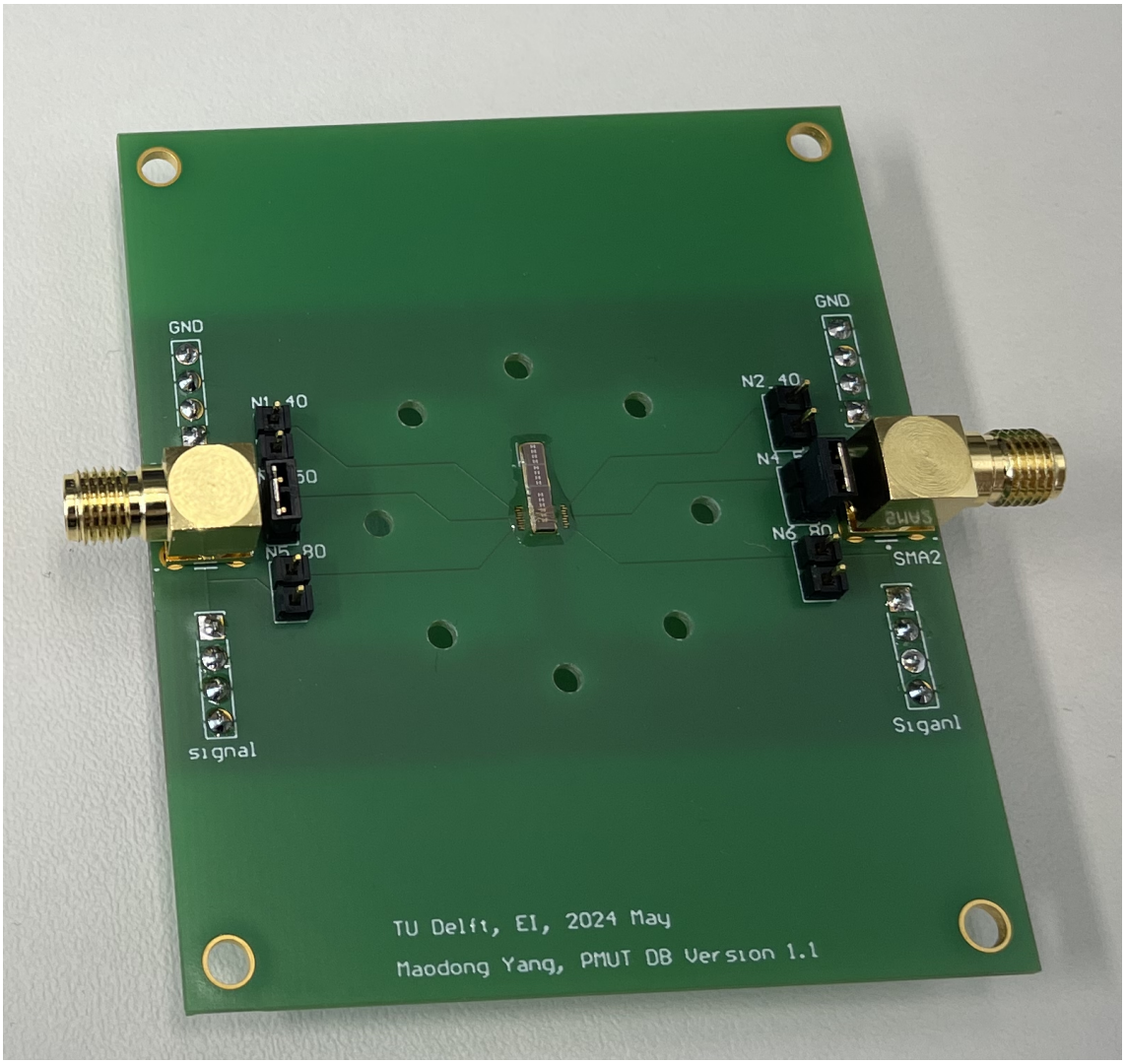

Figure C.2: PCB: daughter board with wire bonding PMUT

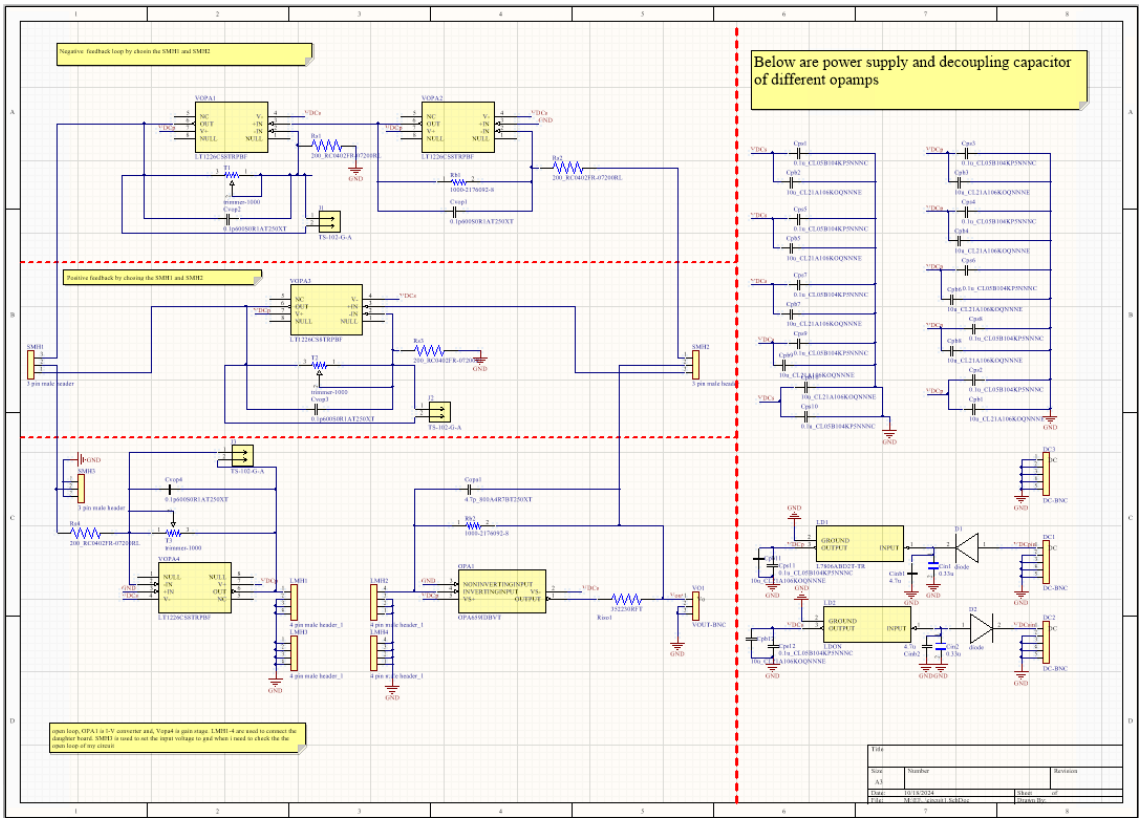

Figure C.3: PCB: motherboard schematic

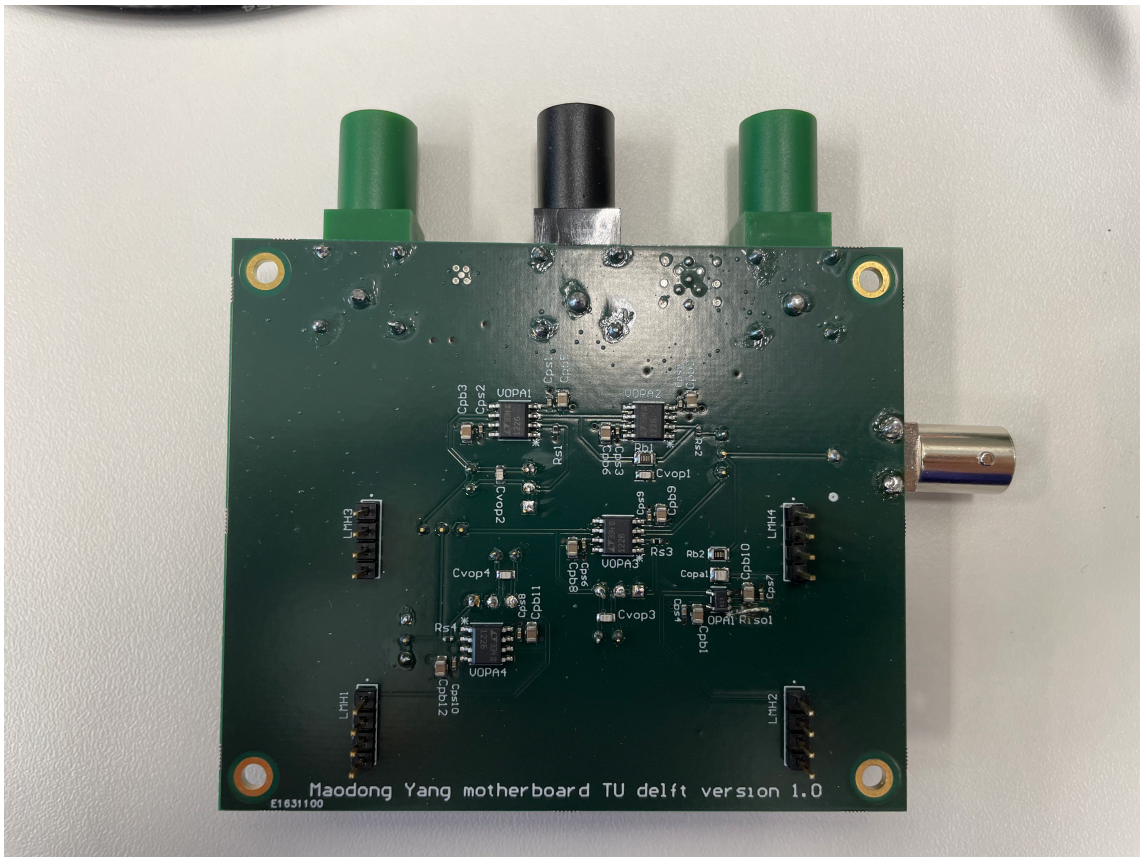

Figure C.4: PCB: motherboard front side

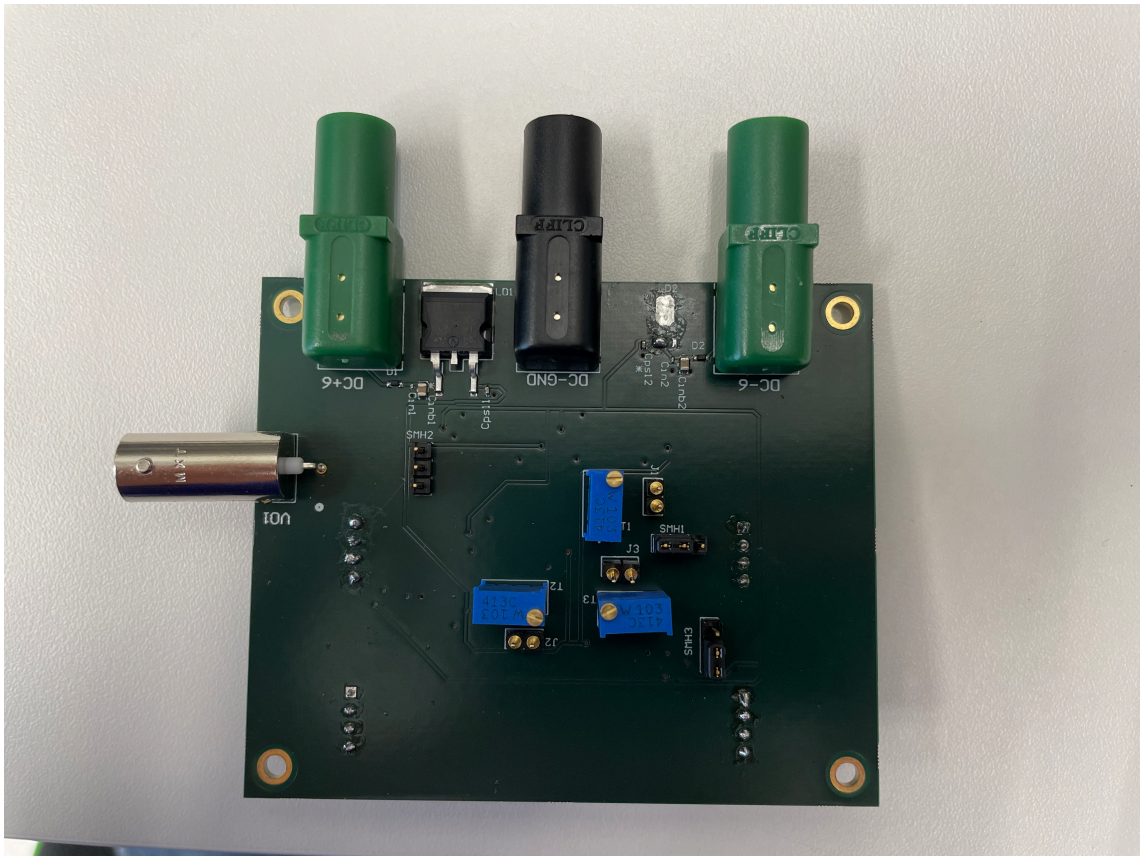

Figure C.5: PCB: motherboard back side